Construction and Function of an Artificial Light Harvesting Antenna Complex

（人工光捕集アンテナ複合体の構築と機能）

ACADEMIC DISSERTATION

RYOICHI TAKAHASHI

髙 橋 良 一

March 2003

Division of Supramolecular Science
Graduate School of Materials Science
Nara Institute of Science and Technology

Contents

List of Schemes

List of Tables

<div align="center">**Chapter 1   General Introduction**</div>

1.1   Natural Photosynthesis

1.1.1   Photosynthetic Reaction

Photosynthetic organisms convert from solar energy to chemical energy with excellent efficiencies. Primary process of photosynthesis is a sequential reaction of light harvesting, excitation energy migration and transfer, charge separation, and charge shift reactions.

1.1.2   Homology for Reaction Center Complexes

In 1984, the structure of the photosynthetic reaction center complex was revealed from photosynthetic purple bacterium *Rhodopseudomonas viridis* (Deisenhofer *et al.*, 1984). This reaction center complex is composed of four protein subunits, and of 14 cofactors. The protein subunits are called H (heavy), M (medium), L (light), and cytochrome; the names H, M, and L were chosen according to the apparent molecular weights of the subunits, as determined by electrophoresis. The core of the complex is formed by the subunits L and M, and their associated cofactors: four bacteriochlorophyll-*b*, two bacteriopheophytin-*b*, one nonheme iron, two quinones, one carotenoid. This core part contains a dimeric structure of (bacterio)chlorophylls which are separated at a distance

of ca. 3 Å in a nearly parallel orientation with partial overlap of π-orbitals, i.e. a slipped-cofacial orientation and generally called a "special pair". Other two bacteriochlorophyll-b, two bacteriopheophytin-b, and two quinones are arranged in pseudo-C_2 symmetry in the core part. These cofactors arrangement are commonly observed in other photosynthetic organisms (Blankenship, 2002). Accordingly, there are homology of the cofactors arrangement in the core part of the reaction center complexes in the photosynthetic organisms.

1.1.3 Heterogeneity for Light Harvesting Complexes

The first event of photosynthetic reaction starts at absorbing light by light harvesting antenna complexes around the reaction center complex. These structures of the light harvesting antenna complexes are rich in diversity (Blankenship, 2002), differently from the structure of the reaction center complexes.

1.1.4 Light Harvesting Complexes of Photosynthetic Purple Bacteria

The structures of the light harvesting complexes (LH1, LH2, and LH3) in photosynthetic purple bacteria have been determined by X-ray crystallographies (McDermott *et al.*, 1995; Koepke *et al.*, 1996; McLuskey *et al*, 2001) and electron

microscopies (Karrasch *et al.*, 1995; Savage *et al.*, 1996; Walz *et al.*, 1998). In antenna complexes in these bacteria, 18 or 16 bacteriochlorophylls are arranged in a macroring with slipped-cofacial orientations by coordination of imidazolyl side chains from transmembrane α-helices in B850, and 9 or 8 bacteriochlorophylls are arranged in a macroring of coplanar orientation in B800. Their special features may refer to the higher ordered barrel structure of complete beauty and scientific significance (**Figure 1.1**). Especially, the key functional unit of B850 is composed of a bacteriochlorophyll-*a* dimer in a slipped-cofacial orientation by coordination from imidazolyl residue to the central magnesium ion, and these dimers are further arranged into a macroring form.
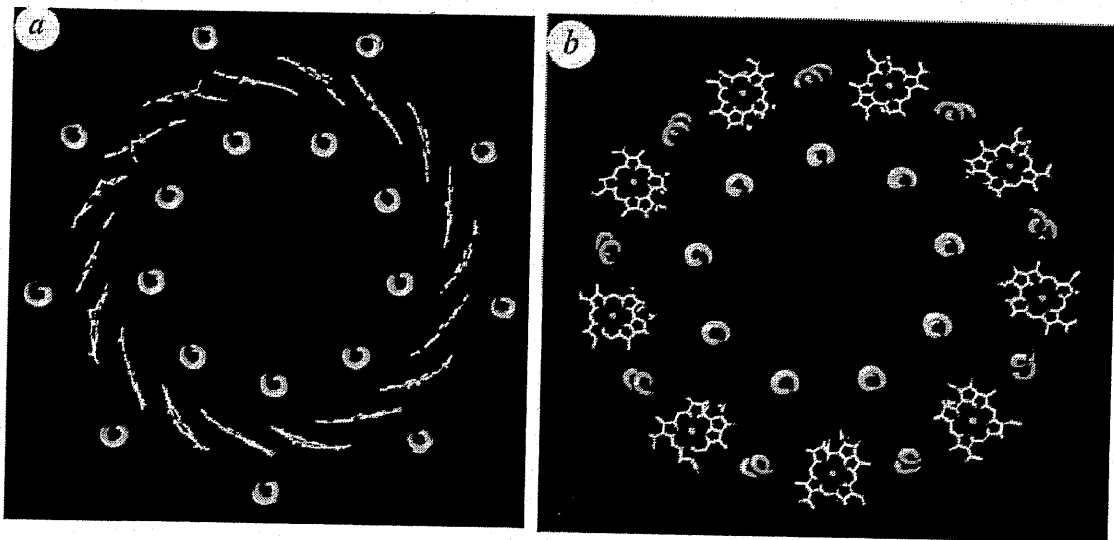
Figure 1.1 The structure of LH2 from *Rhodopseudomonas acidophila* (McDermott *et al.*, 1995). The ring of (a) B850 and (b) B800 bacteriochlorophyll-*a* molecules.

1.2   Artificial Photosynthesis

1.2.1   Porphyrin Chemistry

Porphyrin is a basic framework of photosynthetic pigment chlorophyll and bacteriochlorophyll derivatives, and there are tremendous reports of artificial photosynthesis utilizing porphyrin macrocycle.

1.2.2   Artificial Light Harvesting Antenna Complexes

Efficient strategies had to be explored for the preparation of macroring architecture from novel building blocks and refined approaches, utilizing multistep reaction sometimes with template syntheses. Until now several oligomeric porphyrin rings have been synthesized through both covalent (Sanders, 1996; Sanders, 2000; Li *et al.*, 1999; Mongin *et al.*, 1999) and supramolecular (Knapp *et al.*, 1998; Haycock *et al.*, 2000; Ikeda *et al.*, 2000; Sanders, 2000) approaches toward light harvesting antenna mimics. However, there are practically no systematic studies available yet which would allow a rational design of self-assembled macrorings with the desired properties toward antenna structure and function. To the best of the author's knowledge, there is no example of porphyrin macroring composed of dimer units.

1.3   Previous Research

1.3.1   General Statement

The Kobuke's laboratory has been interested in constructing artificial systems by using the method of self-assembled and/or supramolecular chemistry. The target systems are biosystems especially for energy conversion and signal transduction systems, which have marvelous functions and beautiful structures. The supramolecular approach is considered one of the fascinating area of sciences, because even the use of relatively low cost reagents and less synthetic steps give a basic unit, and further self-assembling to more complicated structure and function.

1.3.2   Special Pair Model

In 1994, Kobuke reported a slipped-cofacial dimer of *meso*-imidazolylporphyrin zinc complex as a model of the special pair of the photosynthetic reaction center complex based on self-organization via ligand-to-metal coordination (**Figure 1.2**) (Kobuke and Miyaji, 1994). This slipped-cofacial dimer have a large association constant ($K_a > 10^{10}$ M^{-1}) in non-polar organic solvents, composed of complementary coordination bonds between nitrogen atom of imidazolyl group and penta-coordinating zinc ion and π-π stacking interaction between each porphyrin. The resulting supramolecule exhibits a

large splitting of its Soret band through exciton coupling interaction between two

porphyrins oriented in a slipped-cofacial arrangement in a close distance.
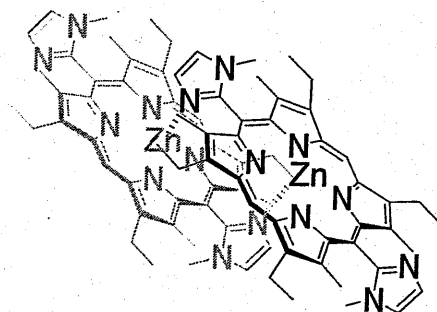
Figure 1.2   The structure of slipped-cofacial dimer.

1.3.3   Magnesium Complex

When using magnesium ion as a central metal of porphyrin instead of zinc ion, a

magnesium complex affords further elongation of imidazolylporphyrins (Kobuke and

Miyaji, 1996). Typical magnesium porphyrin, tetraphenylporphyrinatomagnesium(II)

(MgTPP), binds a first imidazole with a binding constant K_1 of 10^4–10^5 M^{-1} and second

imidazole with a binding constant K_2 of about 1 M^{-1} (Sanders *et al.*, 2000b). The second

binding is less favorable in part because the penta-coordinate magnesium ion is out of

plane. Therefore, the magnesium complex of imidazolylporphyrin has also a relatively

small hexa-coordination property to penta-coordination one, and affords a few

aggregation number of imidazolylporphyrins in solution.

1.3.4   *Meso-meso* Linked Porphyrin Array

To elongate each imidazolylporphyrin, two approaches are considered. The first is using stable hexa-coordinating metal ion as the porphyrin central metal. For example, iron, cobalt and ruthenium are considered as metal ions to give stable hexa-coordination, but these ions are not suitable for the model of early events of photosynthesis because these metalloporphyrins have a fluorescence quenching property. The second is using zinc complex of covalently attached porphyrin dimer. Previously, *meso*-position, opposite to the connecting site of imidazole group, was directly linked to each other and *meso-meso* bis(imidazolyl)porphyrin dimer gave a giant porphyrin array (Ogawa and Kobuke, 2000). This *meso-meso* directly linked bis(imidazolyl)porphyrin dimer have a fluorescence emissive and anticipated as a photoelectric molecular wire.

1.3.5   Further Applications toward Artificial Photosynthesis

Until now, the Kobuke's laboratory has reported many applications of imidazolylporphyrin assembly. 5,15-bis(imidazol-4-yl)-10,20-bis(4-dodecyloxyphenyl)-porphyrin yields supramolecular assembly through imidazole–imidazole hydrogen bonding (Nagata *et al.*, 2000). This supramolecular assemblies exhibit efficient excited

energy transfer followed by electron transfer to quenchers in a non-polar toluene solution.

5,15-Bis(imidazol-4-yl)-10,20-bis(ω-carboxyalkyloxyphenyl)porphyrin, replacing hydrophobic terminal groups into hydrophilic carboxyl groups, was assembled in water to form liposomal dispersions without any lipids (Nagata *et al.*, 2001). This porphyrin assembled in liposomal membranes is expected to interesting materials in view of realizing functions of light harvesting, light induced charge separation, and electron transfer reactions across the membrane. Further, imidazolylporphyrins have been applied to self-assembled monolayer and self-assembled multilayer systems toward organic photovoltaic cell (Nomoto and Kobuke, 2002). Accumulation of imidazolylporphyrins by using ligand-to-metal supramolecular method forms a chain structure and leads to significant increases of light absorption in the visible light region and to large photocurrents generation.

1.3.6   Macroring Assembly towards Artificial Antenna Complex

In my research project in doctoral course is to construct of an artificial light harvesting complex of the LHs of photosynthetic purple bacteria, and to unveil the relation between structure and function. In order to fix chromophores in a certain geometrical arrangement, porphyrins have been connected by rigid aromatic spacers to

avoid the ambiguity arising from conformational mobilities. To accomplish such the

request, a gable porphyrin motif was adopted as a building block. Gable porphyrin is a

1,3-phenylene bridged porphyrin dimer, first reported by Tabushi *et al.* (Tabushi and

Sasaki, 1982; Tabushi *et al.*, 1985). In my project, introducing imidazole group to the

meso-positions of each porphyrin, positions opposite to the phenylene bridging sites. The

gable porphyrin motif fixes each porphyrin in 120° as an orientation angle.
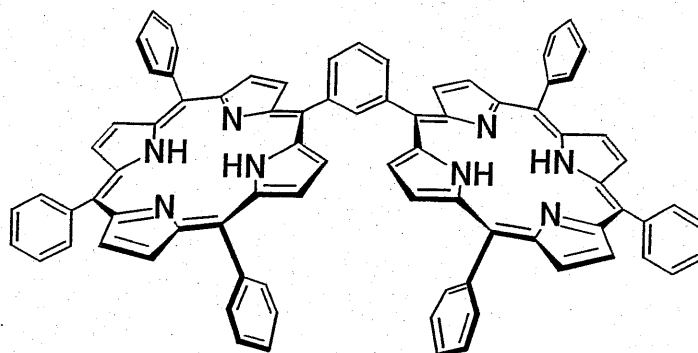
Figure 1.3   The structure of gable porphyrin

This thesis is composed of 5 chapters indicated below:

Chapter 1   General Introduction

This chapter is a general introduction of this thesis and describes about the field, purpose, and contents of this study. Firstly, natural photosynthetic systems were outlined especially in view of light harvesting antenna systems. Next, artificial light harvesting antenna systems by using chemical approach were introduced. Finally, a background of this project was described based on previous reports from the Kobuke's laboratory.

Chapter 2   Synthesis of Free Base Gable Porphyrin

Synthesis and structural determination of a novel free base gable porphyrin were described in this chapter. This gable porphyrin has two imidazolyl substitutents at the apsis of each *meso*-position. The porphyrin syntheses were undertaken according to the Lindsey's approach. Further, a side reaction, scrambling reaction at *meso*-position, during the porphyrin syntheses was described. By choosing appropriate peripheral substituents the side reaction was suppressed, and analytically pure free base bis(imidazolyl) gable porphyrin was obtained. This compound was analyzed in detail by nuclear magnetic resonance measurements and thermodynamic parameters about atropisomers were determined.

Chapter 3.   Formation of Macrocyclic Structure from Zinc(II) Gable Porphyrins

This chapter describes on construction of ring shaped molecular assembly, using a reorganization methods. After zinc(II) insertion to free base gable porphyrin, broad molecular weight distribution was observed by gel permeation chromatography. Reorganizations of the molecular assembly were performed by dissociation and reassociation of molecular assembly, accompanied by the addition and removal of coordinating solvent, respectively, at high dilution conditions. As a result, molecular weight distribution was almost completely convergent to two components. Further structural determination was described both in solid and in solution states. The results of probe microscopies (atomic force microscopy and scanning tunneling microscopy) and small-angle X-ray scattering measurements were described.

Chapter 4.   Antenna Function of Zinc(II) Gable Porphyrins

This chapter describes evaluation of light harvesting antenna function of macroring of gable porphyrins. The photophysical antenna function of the macroring arrays was evaluated by using steady state spectroscopic measurements. Especially, fluorescence quenching experiments revealed excitonic energy migration in the macroring arrays.

Chapter 5.   General Conclusion

This chapter describes general conclusions of this thesis and summarizes the results obtained in this study. Further applications of this study were mentioned by practical combination of our supramolecular science.

Chapter 2   Synthesis of Free Base Gable Porphyrin

2.1   Molecular Design

The structural unit of the building block is bis(1-methylimidazolyl)porphyrin dimer as shown in **Figure 2.1**. The most important point is introducing of two 1-methylimidazolyl groups to the opposite sites to the phenylene bridging site. Further, this molecular unit was designed by keeping two basic points in mind. Firstly, a bis(1-methylimidazolyl)porphyrinatozinc(II) dimer motif (Kobuke and Miyaji, 1994; Ogawa and Kobuke, 2000) was employed as the basic construction unit, because it satisfies perfectly the functional requisites of the light harvesting dimer unit, in view of the distance and the orientation of chromophores, and imidazolyl to zinc coordination free from excitation energy quenching by central metal ion. Secondly, the ring structure was provided by connecting two mono(imidazolyl)porphyrinatozinc(II) with a 1,3-phenylene spacer. 1,3-phenylene bridged porphyrin dimer is called "gable porphyrin" first reported by Tabushi *et al.* in 1982 (Tabushi and Sasaki, 1982; Tabushi *et al.*, 1985). This porphyrin is also the first porphyrin dimer in which each porphyrin is fixed rigidly with its spatial orientation of 120°. In contrast to the *meso-meso*-coupled bis(1-methylimidazolyl)porphyrinatozinc(II), which grows linearly into a giant porphyrin array (Ogawa and Kobuke, 2000), the spatial orientation with 120° is expected to give a

closed ring under appropriate conditions. If all these designs work perfectly, a dodecaporphyrin array composed of hexakis(gable porphyrin) would be constructed as shown in **Figure 2.2**. This porphyrin macroring array have a barrel structure with center-to-center distances of 6.1 and 11.0 Å, in a close analogy to those of the light harvesting complexes of photosynthetic purple bacteria. The remaining four *meso*-positions are introduced by aryl or alkyl groups with long alkyl chain to give the solubility of porphyrin arrays in organic solvents.
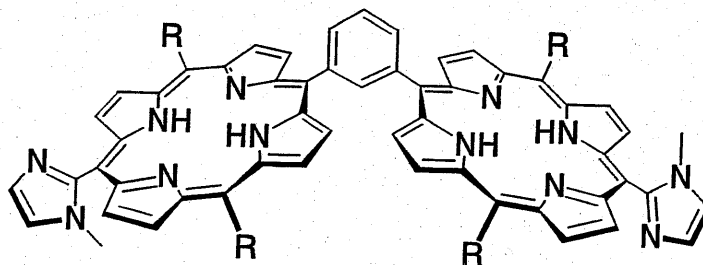
Figure 2.1 The molecular structure of bis(1-methylimidazolyl) gable porphyrin.
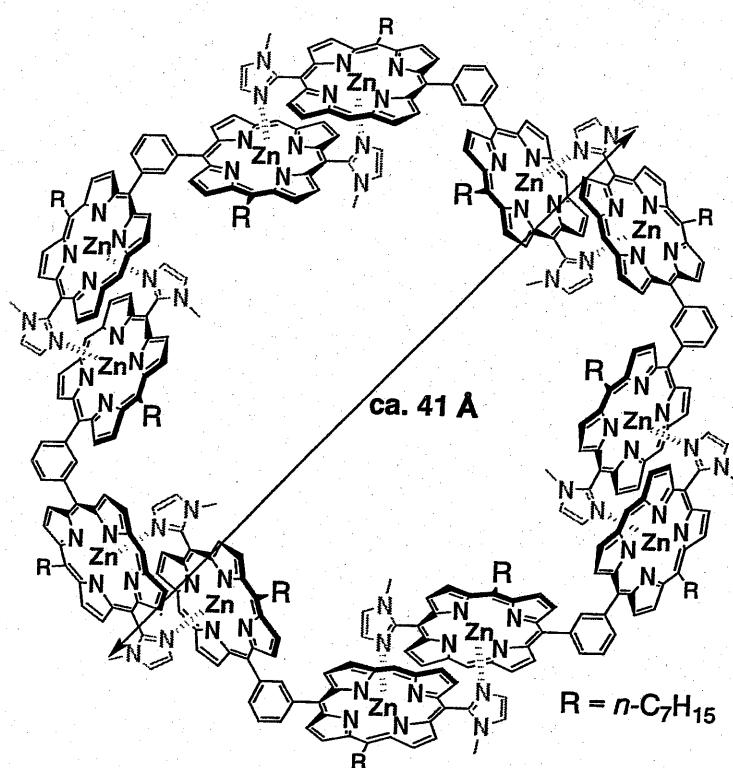
Figure 2.2 The structure of hexakis(gable porphyrin) macroring array.

2.2   Synthesis of Dipyrromethanes

2.2.1   General Statement
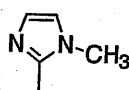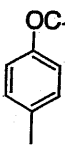
Dipyrromethane derivatives are very useful precursors in the synthesis of 5,15-disubstituted porphyrins, *trans*-porphyrins. While several methods of dipyrromethane synthesis were reported, especially Lindsey *et al.* have explored the dipyrromethane chemistry most efficiently and reported detailed preparations, purifications, and their applications to the corresponding porphyrin (Lee and Lindsey, 1994; Littler *et al.*, 1999). Accordingly, the author referred to their reports in the synthesis of following several dipyrromethanes (Scheme 2.1). Excess amount of pyrrole, 40-fold to each aldehyde except for bis-dipyrromethane 1 case (25.7-fold of pyrrole), was used as both the reagent and solvent, and all reactions were catalyzed by small amount of trifluoroacetic acid (TFA) at room temperature. All reactions were neutralized with 0.1 M sodium hydroxide aqueous solution, and excess pyrrole was recovered under reduced pressure, and further purification was performed by silica gel column chromatography or vacuum distillation.

In 1999 Lindsey *et al.* reported a refined method of synthesis and purification of *meso*-substituted dipyrromethanes (Littler *et al.*, 1999), and they described N-confused dipyrromethane (2,3'-dipyrromethane) and tripyrrane as byproducts of dipyrromethane (Scheme 2.2). After receiving their reports, the author observed the tripyrrane

component as the main byproduct in the *meso*-alkyldipyrromethane syntheses by TLC and ^{1}H-NMR analyses (data not shown), while the N-confused dipyrromethane component could neither be observed and nor identified in these reactions. Instead, another component was also observed in the TLC analysis. Although the author could not isolate this component because their paucity and relatively unstable nature to dipyrromethanes, this was considered to be tetrapyrrane from their polarity in the TLC analysis. Condensation of dipyrromethane with aldehyde in a MacDonald type 2 + 2 reaction (Arsenault et al., 1960) prophetically gives a precursor of a 5,15-disubstituted porphyrin. However, in the acid catalyzed porphyrin synthesis, an extensive scrambling reaction is reported to occur, leading to a mixture of porphyrins besides the desired *trans*-porphyrin. This scrambling process frequently observed in open chain polypyrrane condensations is proposed to occur by the acid catalyzed fragmentation of polypyrrane into pyrrolic and azafulvene components (Smith, 1975a). Fortunately, tripyrrane could not give porphyrin byproducts because there are no monopyrrolic components in the reaction system if no scrambling reaction has occurred. In this way, tripyrrane might be a negligible component in the porphyrin condensation reaction derived from aldehydes and dipyrromethanes (Gerasimchuk *et al.*, 1998) unless extra reaction was occurred, while tripyrrane could be utilize to the synthesis of pentaphyrin macrocycles, one of expanded

porphyrins (Rexhausen and Gossauer, 1983). But elimination of tripyrrane by further

purification is preferable, since this component might consume the acid catalyst and give

tar-like polymeric byproducts from oxidized polypyrrane components. Consequently,

each dipyrromethane was purified by silica gel column chromatography or vacuum

distillation to afford analytically pure dipyrromethanes in **1**, **2**, **3**, and **4**, except for **5**

with 80 % purity from ^{1}H-NMR analysis.

Scheme 2.1   Series of dipyrromethanes

meso-(R)dipyrromethane

2 - 5

R	$N{\equiv}N{-}CH_3$	$OC_{12}H_{25}$	$n{-}C_{13}H_{27}$	$n{-}C_7H_{15}$
No.	**2**	**3**	**4**	**5**

Scheme 2.2   Dipyrromethane and byproducts
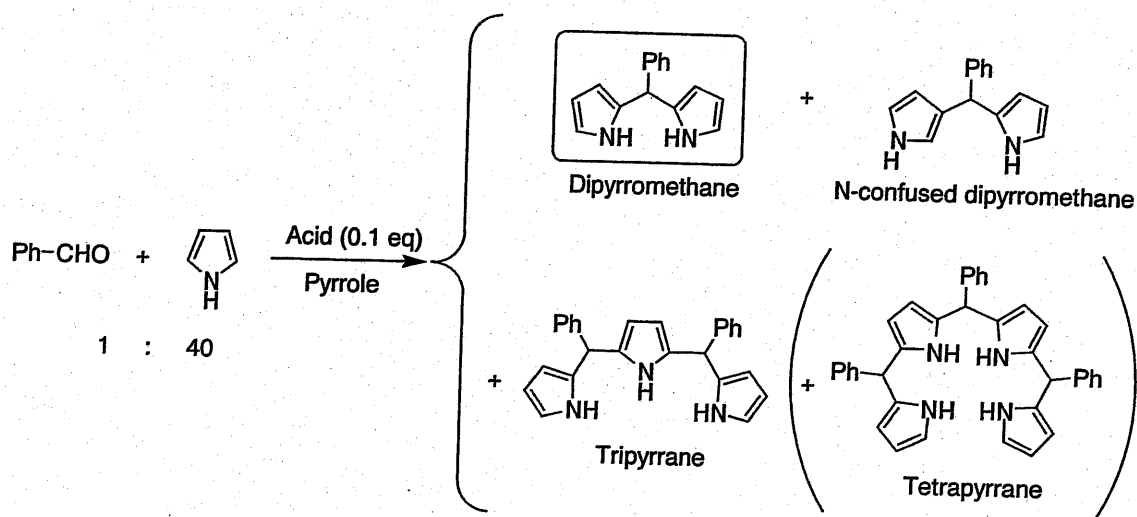
2.2.2   Bis-dipyrromethane

After silica gel column chromatography, two species were observed in isolated 1,3-bis(2,2'-dipyrromethyl)benzene **1** both in the TLC and ^{1}H-NMR analyses. This was readily understood as *meso-* and *racemo-*isomers.

2.2.3   *Meso*-aryldipyrromethane

Meso-(1-methylimidazol-2-yl)dipyrromethane **2** and *meso*-(4-dodecyloxyphen-1-yl)dipyrromethane **3** were purified by silica gel column chromatography. Even after

column chromatography, purified *meso*-(4-dodecyloxyphen-1-yl)dipyrromethane **3**

contained a tripyrrane component from ^{1}H-NMR analysis. However it seems difficult to

elucidate the dipyrromethane purity and tripyrrane contents since they are derived from

same starting materials, and the author distinguished each component quantitatively by

NMR intensity of proton signals at the *meso*-positions (1.000 (1H) at d 5.42 ppm for

dipyrroemethane **3**, 0.399 (2H) at d 5.30 ppm for tripyrrane) (Brückner *et al.*, 1997).

Hence, molar ratio of dipyrromethane **3** to tripyrrane was 1:0.2 and the purity of

dipyrromethane **3** was above 80%. It seems wasteful to perform further purification of

dipyrromethane **3** by column chromatography, since the corresponding tripyrrane are of

relatively close polarities not like other dipyrromethane derivatives from TLC analysis.

Further, other purification methods (e.g. bulb-to-bulb distillation and recrystallization)

seemed difficult to isolation, because of its nonvolatile property and flexible side chains

as seen in *meso*-[4-[2-(Trimethylsilyl)ethoxycarbonyl]phenyl]dipyrromethane (Rao *et al.*,

2000).

2.2.4   *Meso-n*-alkyldipyrromethane

In the synthesis of *n*-alkyldipyrromethanes, the author perused Lindsey's refined

report (Littler *et al.*, 1999). They permitted dipyrromethane synthesis in multi-gram

scales by refining purification method to bulb-to-bulb distillation followed by recrystallization instead of tedious column chromatography. The author could obtain multi-gram n-alkyldipyrromethanes by bulb-to-bulb distillation, according to the refined Lindsey's method except for a pyrrole:aldehyde ratio. Lindsey et $al.$ refined to use the pyrrole:benzaldehyde ratio of 25:1 from compromise idea between isolated yield of dipyrromethane and the price of excessive pyrrole. Although the author utilized their ratio of 40:1, taken into consideration that tetrapentylporphyrin have a maximum yield at one order of diluted condition (10^{-3} M) than a tetaraphenylporphyrin case (10^{-2} M) from pyrrole and corresponding aldehyde (Lindsey et $al.$, 1987). In the synthesis of $meso$-(n-tridecyl)dipyrromethane **4**, deaeration was performed only for pyrrole prior to the addition of n-tetradecanal since argon bubbling to the solution caused overflowing. In the preparation of $meso$-(n-heptyl)dipyrromethane **5**, analytically pure dipyrromethane was obtained in a higher yield (65.5%) than the authentic $meso$-aryldipyrromethane procedure by bulb-to-bulb distillation (Tomohiro et $al.$, 2001).

2.3   Synthesis of Free Base Gable Porphyrin

2.3.1   General Statement

As preliminary experiments, the author had referenced two reports of synthesis of

gable type porphyrins, (1) Sessler group (Sessler *et al.*, 1986) and (2) Maruyama group

(Osuka *et al.*, 1986). According to these reports, the author designed two synthetic

routes: (1) utilizing one aldehyde and two dipyrromethane (**Scheme 2.3**) and (2) utilizing

two aldehydes and one dipyrromethane (**Scheme 2.4**).

Scheme 2.3   Route 1

Bis-dipyrromethane

1   **2**

gable porphyrin   R =

Scheme 2.4   Route 2

3

gable porphyrin   R =
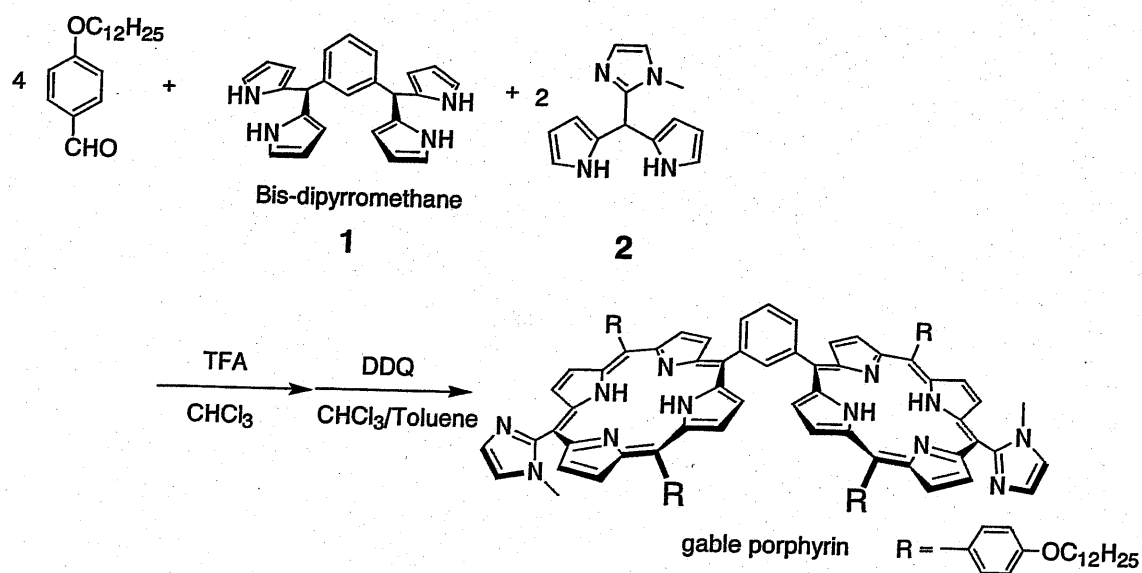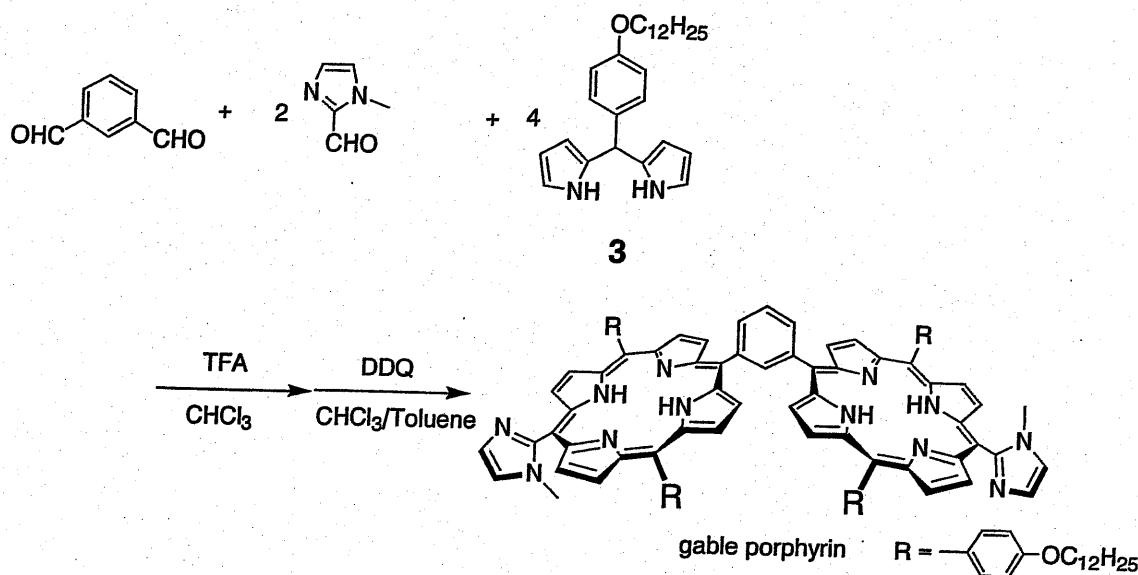
The author utilized a modified Lindsey's method in the following porphyrin syntheses, because 5,5'-free dipyrromethanes with various *meso*-substituents seems to be more readily prepared than the corresponding 5,5'-diformyldipyrromethane analogs utilized in the MacDonald's approach (**Scheme 2.5**). This Lindsey's method is well established for the synthesis of *meso*-substituted porphyrins and composed of one-pot two-step reactions under mild conditions *via* porphyrinogen as an intermediate precursor of porphyrin macrocycle. Various reaction conditions (e.g. reagents ratio, concentration, the kind of acid catalysts and reaction time) were employed in an effort to optimize the condensation and oxidation reaction. TFA or boron trifluoride etherate diethyl ether complex (BF$_3$·Et$_2$O), and *p*-chloranil (TCQ) or 2,3-dichloro-5,6-dicyano-*p*-benzoquinone (DDQ)

were used as an acid catalyst and an oxidant, respectively.

Scheme 2.5   Lindsey's method

meso-(R$_1$)dipyrromethane   Porphyrinogen   Porphyrin

Acid = TFA or BF$_3$·OEt$_2$,   DDQ =
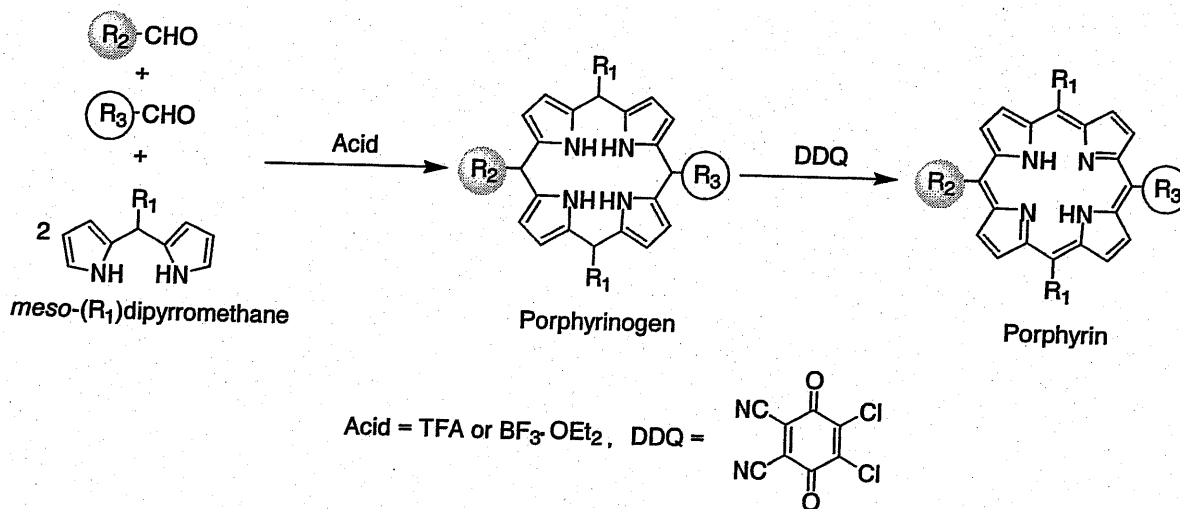
2.3.2   Tetraalkoxyphenyl Gable Porphyrin

The author explored the synthesis of tetaraalkoxyphenyl gable porphyrin according to both **Scheme 2.3** and **2.4**. According to **Scheme 2.3**, acid catalyzed condensation of 4-dodecyloxybenzaldehyde with two dipyrromethanes, 1,3-bis(2,2'-dipyrromethyl)benzene **1** and meso-(1-methylimidazol-2-yl)dipyrromethane **2**, followed by oxidation afforded the crude products which were analyzed by TLC and MALDI-TOF MS spectrometry. As a result, several porphyrin-like components, red fluorescent spots by long wavelength UV irradiation at 365 nm, were observed other than reference compound 5,15-bis(1-methylimidazol-2-yl)-10,20-bis(4-dodecyloxyphenyl)porphyrin **A** in the TLC analysis.

Meanwhile the gable porphyrin peak could not be observed by MALDI-TOF MS spectrometry. These additional components were also identified as 5-(1-methylimidazol-2-yl)-10,15,20-tris(4-dodecyloxyphenyl)porphyrin **B** and 5,10,15,20-tetrakis(4-dodecyloxyphenyl)porphyrin **C** by MALDI-TOF MS analysis (**Figure 2.3**). They seemed derived from the scrambling reaction of *meso*-substituents (Lindsey *et al.*, 1987). According to **Scheme 2.4**, the crude products of acid catalyzed condensation of *meso*-(4-dodecyloxyphen-1-yl)dipyrromethane **3** with two aldehydes, isophthalaldehyde and 1-methyl-2-imidazolecarbaldehyde, followed by oxidation were analyzed by TLC and MALDI-TOF MS spectrometry. Similar to the results of **Scheme 2.3**, several porphyrin-like components were observed in TLC, and these were ascribed to the possible product **A** and the byproducts **B** and **C** rather than the gable porphyrin by MALDI-TOF MS spectrometry. In order to find the appropriate reaction condition for generating gable porphyrin by suppressing the scrambling reaction, the author monitored the time course of the acid catalyzed condensation by TFA. By using **Scheme 2.4** as a model reaction, the time course was monitored by MALDI-TOF MS spectrometry. As a result, **A** and **B** were detected at 15 min, and **A**, **B**, and **C** were detected at 75 min, and the author could not detect the gable porphyrin. It was concluded that the scrambling reaction occurred at initial condensation stage and depended on the time course.
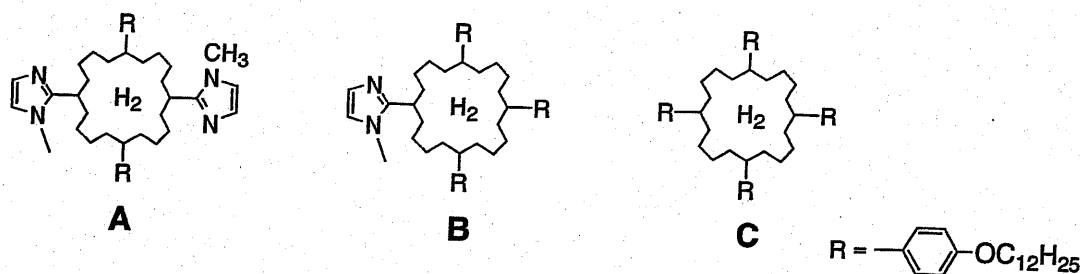
Figure 2.3   Byproducts A, B, and C.

2.3.3   Scrambling Reaction at *Meso*-position

Since a long time ago the scrambling reaction of *meso*-substituents during course of the porphyrin syntheses was known as "jumbling" or "redistribution" reactions and yielded a mixture of several different porphyrins (Smith, 1975). This scrambling come from the acid catalyzed fragmentation of polypyrrane (describe above and **Scheme 2.6**), and also occurred from β–alkyl substituted pyrrole derivative, 3,3',4,4'-tetramethyl-2,2'-dipyrrylmethane (Gunter and Mander, 1981). To avoid such scrambling reaction, extremely mild cyclization conditions and/or different strategies were required (Smith, 1975). Recently Lindsey *et al.* explored further refinement of reaction conditions that eliminated scrambling for condensations. Unfortunately, in this refinement, suppression of the scrambling reactions was restricted only to sterically hindered dipyrromethanes, such as *meso*-mesityldipyrromethane (Littler *et al.*, 1999), and an alternative route was proposed in the preparation of *trans*-porphyrins bearing sterically unhindered

substituents by the self-condensation of a dipyrromethanecarbinol (Rao *et al.*, 2000). On the other hand, the irreversible scrambling reaction was reported in the combination of the alkyl aldehyde and pyrrole condensation in their pioneering work (Lindsey *et al.*, 1987). The author employed the latter description as the most convenient modifications and examined in detail the syntheses of *meso-n*-alkyl substituted porphyrins.

Scheme 2.6 Scrambling reaction

Polypyrrane **a**   Pyrrolic **b**   New polypyrrane **d**

Porphyrinogen **e**   Porphyrin **f**
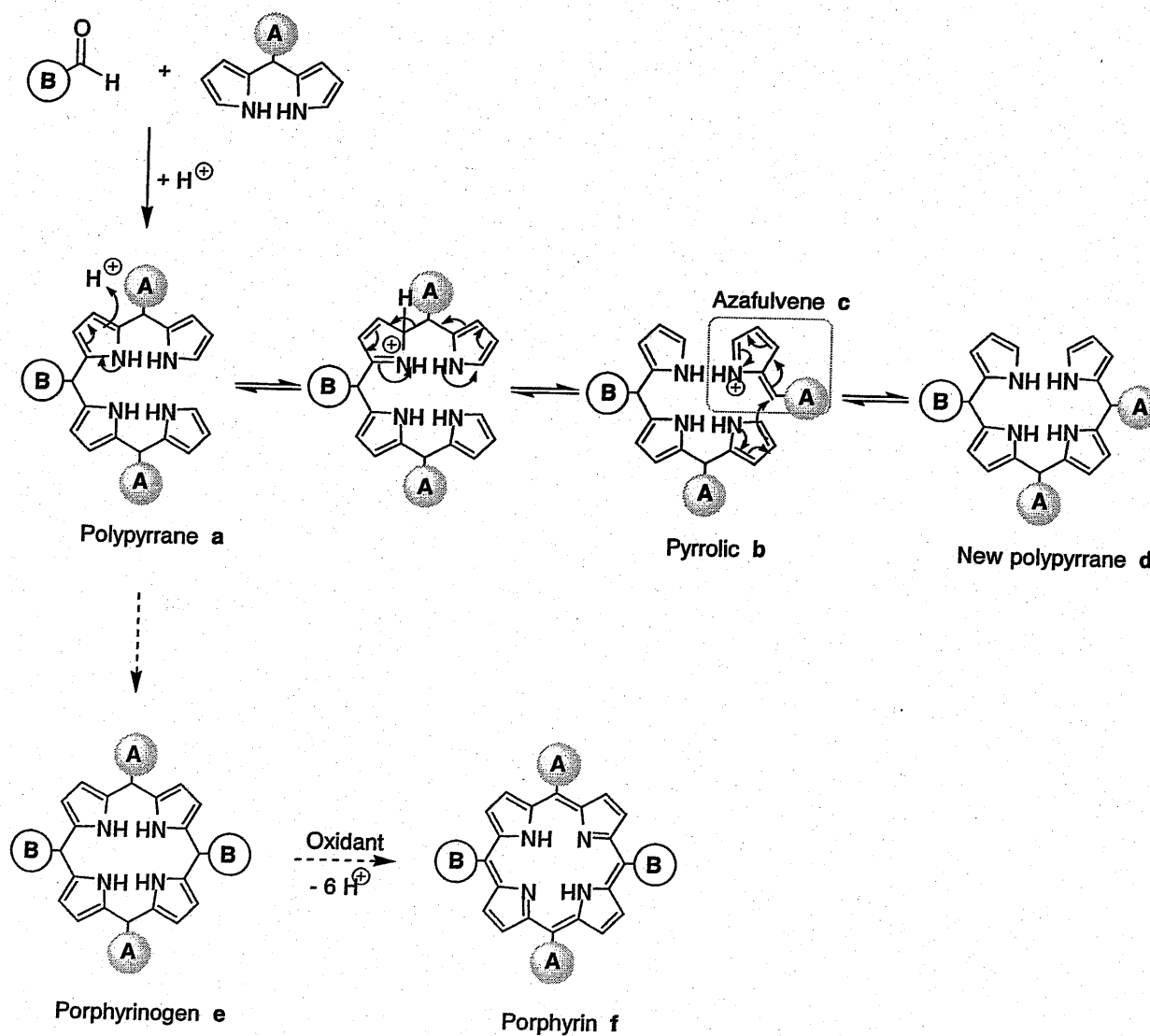
2.3.4   Tetra(*n*-tridecyl) Gable Porphyrin

At first the author utilized *meso-(n*-tridecyl)dipyrromethane **4** as a starting material.

Similarly to **Scheme 2.4**, acid catalyzed condensation of *meso-(n*-tridecyl)dipyrromethane **4** with two aldehydes, isophthalaldehyde and 1-methyl-2-imidazolecarbaldehyde, followed by oxidation were analyzed by TLC and MALDI-TOF MS spectrometry. In the crude products, one major component with several minor spots were observed except for the possible byproduct, 5,15-bis(1-methylimidazol-2-yl)-10,20-bis(*n*-tridecyl)porphyrin **6**, by TLC analysis and gable porphyrin peak was detected with negligible amounts of scrambling byproducts by MALDI-TOF MS. Three column chromatographies, (i.e. silica gel, basic alumina, and size exclusion columns) were sequentially applied and the major porphyrin component was isolated. Surprisingly the major component was ascribed to 5-(1-methylimidazol-2-yl)-15-(3-formylphen-1yl)-10,20-bis(*n*-tridecyl)porphyrin **7** instead of the designed gable porphyrin from MALDI-TOF MS and ¹H-NMR analyses in a 6.1% isolated yield. Furthermore trace amounts of components, eluted faster than **7**, were ascribed to the mixture of porphyrin dimers, objective gable porphyrin **8** and mono(1-methylimidazolyl)-mono(3-formylphenyl)porphyrin dimer **G** (**Figure 2.4**). From this first trial, porphyrin monomers (**6** and **7**) and trace amounts of porphyrin dimers (**8** and **G**) were obtained as reaction

28
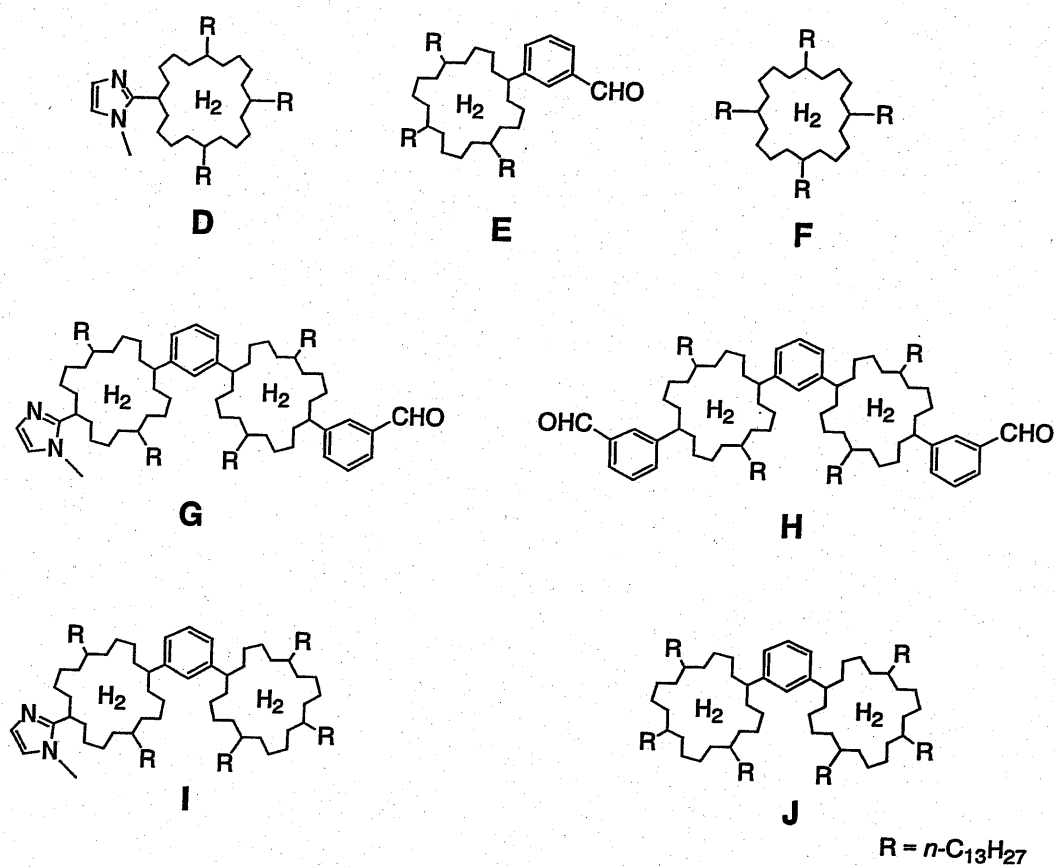
products.

Figure 2.4   Byproducts D, E, F, G, H, I, and J.

Since the byproduct 7 has a potential to be converted to gable porphyrin 8, a wide variety of reaction conditions were examined to convert 7 to the gable porphyrin in the same reaction series, i.e. "one step route" (Scheme 2.7 and Table 2.1). As a result of these trials, the byproduct 7 survived during the courses of one step route. Further addition of TFA or using $BF_3 \cdot Et_2O$ instead of TFA caused the scrambling reaction and afforded further undesirable byproduct D and E.

Based on the fact that the scrambling reaction may not occur once oxidized, the byproduct **7** was treated as the starting material of gable porphyrin. Therefore, **7** was isolated as a building block of gable porphyrin and subjected to another cyclization reaction in a so-called "two steps route" (**Scheme 2.8** and **Table 2.2**). Because of less reactivity of the starting material **7** in this second step, the author experienced requirements that taking long condensation time and/or adding excess amounts of TFA to consume **7**. While excess amounts of TFA could consume formyl substituted porphyrins (**7, E, G,** and **H**), the scrambling reaction products **D, F, I,** and **J** were generated (**Figure 2.4**). Therefore objective gable porphyrin could not be isolated by this reaction system.

Scheme 2.7 First step

Acid = TFA or BF$_3 \cdot$O(Et)$_2$ Formylporphyrin   R = n-C$_{13}$H$_{27}$

7
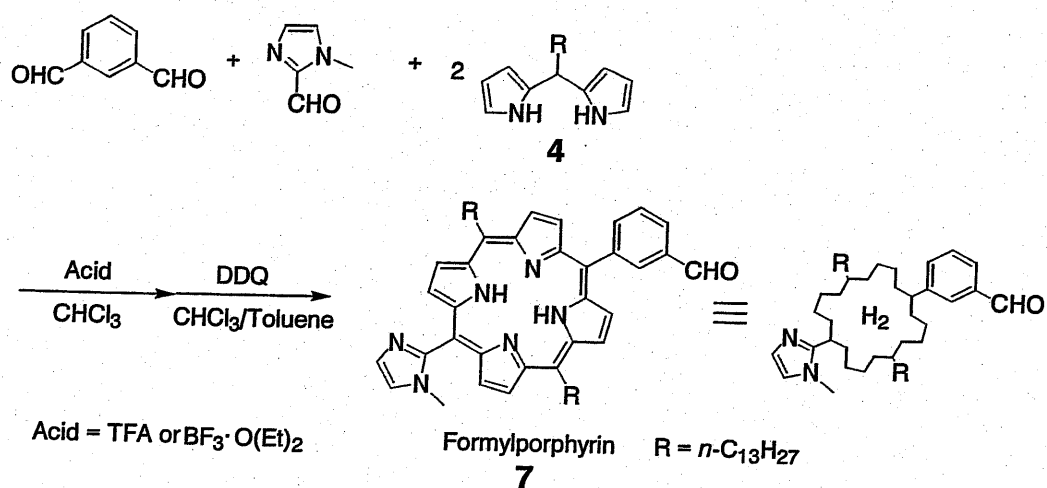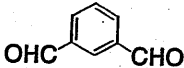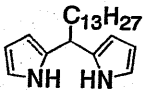
Table 2.1 First step

Run number	OHC⬡CHO	⬠N-methyl CHO	C$_{13}$H$_{27}$ dipyrromethane	Acid	DDQ	Condensation time	Exchange reaction
1	1 eq	2 eq	4 eq	4 +8 eq	6 eq	6 h	—
2	2 eq	2 eq	4 eq	2 eq	6 eq	14 h	—
3	3 eq	2 eq	4 eq	6 eq	6 eq	3 h	+
4	2 eq	2 eq	4 eq	8 eq	6 eq	2 h	+
5	2 eq	2 eq	4 eq	1.32 eq	6 eq	2 h	+
6	0 eq	2 eq	2 eq	2 eq	3 eq	23 h	—
7	1 eq	8 eq	10 eq	6 eq	15 eq	8 h	—
8	1 eq	8 eq	10 eq	6 eq	15 eq	24 h	—

Scheme 2.8   Second step

gable porphyrin   R = n-C₁₃H₂₇

Table 2.2   Second step

R = n-C₁₃H₂₇
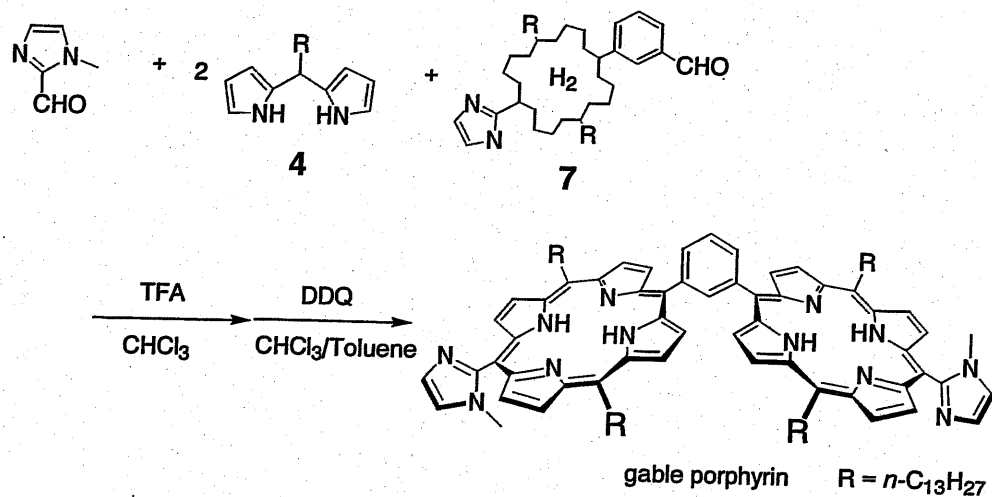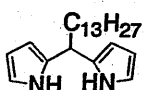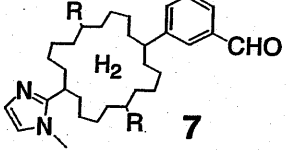
Run number	N–N–CHO imidazole	C₁₃H₂₇ dipyrromethane (4)	7	TFA	DDQ	Condensation time	Exchange reaction	Survival of 7
9	1 eq	2 eq	1 eq	1 eq	3 eq	46 h	−	+
10	1 eq	2 eq	< 1 eq	6 eq	3 eq	2 h	+	+
11	1.5 eq	3 eq	< 1 eq	6 eq	4.5 eq	49 h	+	−
12	5 eq	10 eq	1 eq	18 eq	15 eq	49 h	+	−
13	1.7 eq	3.4 eq	< 1 eq	40 eq	5.1 eq	2 h	+	−

2.3.5 Tetra(*n*-heptyl) Gable Porphyrin

Meso-(*n*-heptyl)dipyrromethane **5** could be obtained in an analytically pure form in a high yield (65.5%) by bulb-to-bulb distillation (Tomohiro *et al.*, 2001). The author finally utilized this dipyrromethane **5** and succeeded in the synthesis of bis(imidazolyl) gable porphyrin **11** by using the previous knowledge about the scrambling reaction. Purification was achieved by three kinds of chromatography (basic alumina, silica gel, and size exclusion chromatography), and analytically pure free base gable porphyrin **11** was obtained in a 2.1% total yield of the first and second steps.

2.4 Characterization of Free Base Gable Porphyrin

2.4.1 Nuclear Magnetic Resonance Spectroscopy

From 600 MHz ^{1}H-NMR measurement of this gable porphyrin **11**, three atropisomers were observed in a 1:2:1 statistical ratio (**Figure 2.5**).
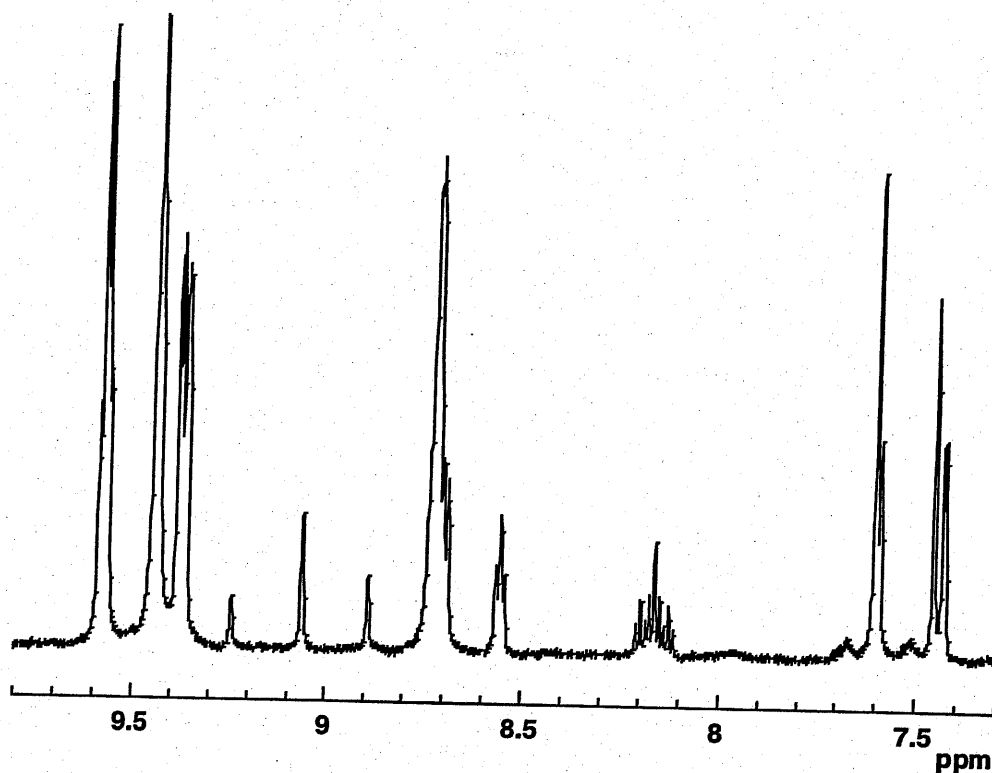
Figure 2.5 600 MHz ^{1}H-NMR spectrum of free base gable porphyrin **11** in $(CDCl_2)_2$ at room temperature.

2.4.2 Dynamic Nuclear Magnetic Resonance Spectroscopy

The author examined the formation and isomerization barrier of atropisomers of bis(1-methylimidazolyl)porphyrins. The steric hindrance between 1-methyl group of imidazolyl ring and β-protons of pyrrole rings causes a perpendicular orientation of the imidazolyl group to the porphyrin plane. The atropisomers could be distinguished from different chemical shifts, induced by a ring current effect between the imidazolyl group and the porphyrin plane in NMR spectra. If the 1-methylimidazolyl group rotates freely,

one would expect one single NMR peak for the 1-methyl group. However, the actual NMR spectrum gave two peaks instead of one peak, and this is thought to result from the atropisomers being in magnetically nonequivalent environments.

The rate of exchange between atropisomers increases as the temperature is increased, and the lifetime of each state thus decreases and the corresponding NMR signals are broadened. At temperatures below the coalescence temperature few molecules have sufficient energy to prevail against the rotational barrier. At temperatures higher than the coalescence temperature, many molecules have enough thermal energy to overcome the barrier and then free rotation occurs. In the case of free base gable porphyrin 11, a plot of ln k versus $1/T$ (Eyring plot) afforded a value for the activation energy E_a for the rotational isomerization (**Figure 2.6**). Using values of k extending over the variable temperature range, 373–301 K, the activation energy $\Delta G_{298\,K}^{\ddagger}$ at 298 K was obtained as 71.1 kJ mol^{-1}. In the case of *meso*-phenyl and *meso-o*-fluoro-phenyl rotations were reported as 45 ± 5 and 93.2 ± 1.3 kJ mol^{-1} at 210 and 298 K, respectively (Crossley *et al.*, 1987). Further, in the case of *trans*-bis(1-methylimidazol-2-yl)porphyrin 9 no coalescence peak was observed at temperature lower than 373K. Considering these points, gable porphyrin 11 might rotate not around the 1-methylimidazolyl side, but around the phenyl ring side. Relatively large activation energy $\Delta G^{\ddagger}$ of 11 to one of *meso-*

phenylporphyrin may come from slower diffusion of bulky 3-pophyrinylphenyl

substituent.
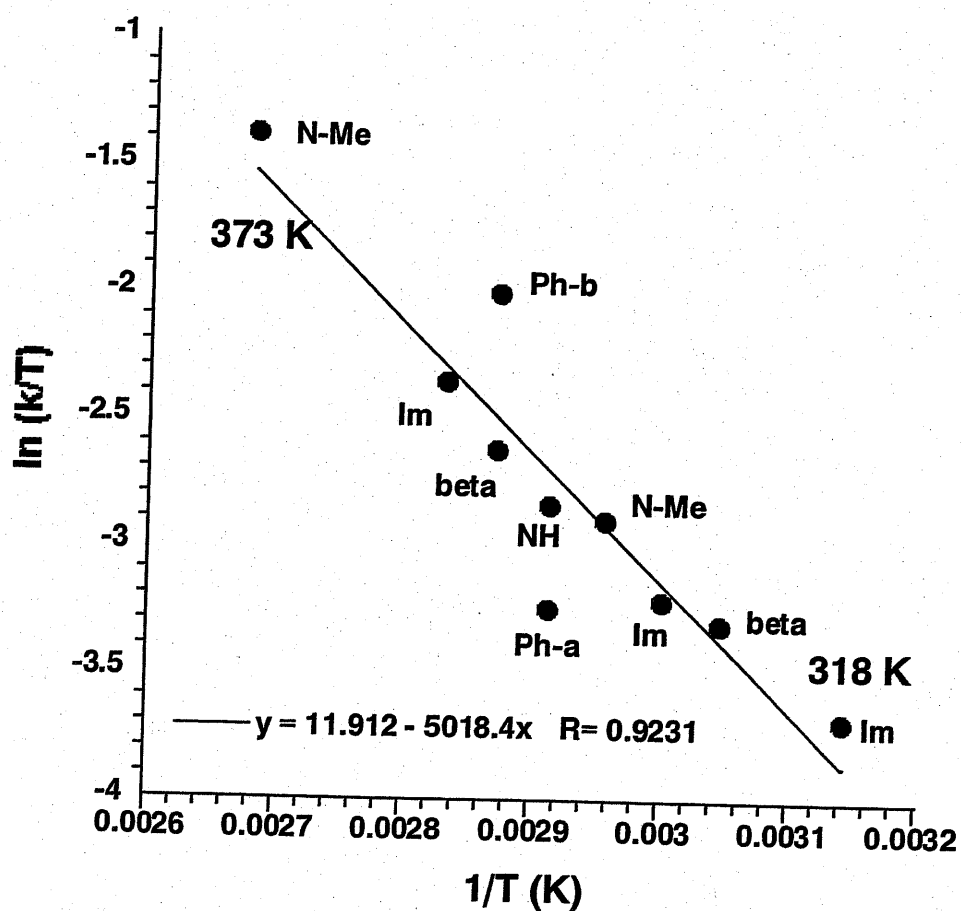
Figure 2.6 Eyring plot for free base gable porphyrin **11** by variable temperature NMR measurements in $(CDCl_2)_2$.

2.5   Experimental Section

2.5.1   Reagents

All reagents were obtained commercially and used without purification.

2.5.2   Nuclear Magnetic Resonance Spectroscopy

Deuterated chloroform ($CDCl_3$) containing tetramethylsilane (TMS) as an internal standard, and deuterated 1,1,2,2-tetrachloroethane (($CDCl_2)_2$) were used.

2.5.3   General Porphyrin Synthesis

Porphyrins (from crude reaction mixtures and/or the succeeding purification) were analyzed by TLC and MALDI-TOF MS with dithranol as a matrix. During the optimization of condensation conditions, minimum amounts of aliquots were pipetted out from the reaction solution followed by oxidation with DDQ, and analyzed by TLC and MALDI-TOF MS. All preparative scale column chromatographies were performed under foil-wrapped open column.

2.5.4   Free base porphyrins in a single step route

The solvent $CHCl_3$ was treated with nitrogen gas bubbling for more than 10 min.

Starting materials, isophthalaldehyde (201 mg, 1.5 mmol), 1-methyl-2-imidazolecalbaldehyde (496 mg, 4.5 mmol), and *n*-heptyldipyrromethane **5** (Tomohiro *et al.*, 2001) (1,026 mg, 9 mmol) were dissolved in $CHCl_3$ (375 mL) into a 500 mL one-neck round-bottom flask. TFA catalyst (687 µL, 9 mmol) was added, and the reaction mixture was stirred at room temperature, monitored by silica gel TLC. After isophthalaldehyde was consumed, typically 6 h, *p*-chloranil (2,766 mg, 11.25 mmol) was added using 5 mL toluene, and the solution was stirred for further 2 h. The acid catalyst was neutralized by triethylamine (1,250 µL, 9 mmol), and the solution was poured onto a pad of deactivated basic alumina column. $CHCl_3$ as eluent were added until free base porphyrin components were fully eluted, and the eluent was rotary evaporated to dryness as a porphyrin mixture. The mixture of free base porphyrins were dissolved in a minimum amount of $CHCl_3$, loaded onto silica column(s) ($CHCl_3$, then $CHCl_3$/acetone = 5/1 (v/v)). Three bands were observed with the following composition: (1) monoformylporphyrins (mainly monomer **10**), (2) bis(imidazolyl)porphyrins (mainly dimer **11** and monomer **9**), and (3) bis(imidazolyl)porphyrins (only monomer **9**). After removal of a tar component (quinone species and polypyrromethene impurities), the band (1) was eluted with $CHCl_3$ only, and the bands (2) and (3) were eluted with $CHCl_3$/acetone = 5/1 (v/v). Each fraction was rotary evaporated to dryness and yielded

87 mg, 63 mg, and 190 mg, as the band (1), (2), and (3), respectively. From ^{1}H NMR analysis, the band (1) component were comprised of mainly monomer **10** and small amounts of dimer **11**, 64.8 mg (93.8 μmol; 6.3%) and 22.0 mg (17.6 μmol; 1.2%), respectively.

Further silica gel column purification was achieved for the band (1), and **10** was recycled to the second cyclization step (see below). Final separation of the band (2) was achieved by dissolving the mixture in a minimum amount of benzene (or toluene), and chromatographing the solution on the gel permeation chromatography (GPC) columns. Three bands were observed by an UV lamp (365 nm) irradiation with the following composition: (1)' mainly trimer, higher molecular weight components, and dimer **11**, (2)' mainly dimer **11** and small amounts of trimer and monomer **9**, and (3)' only monomer **9** on the basis of MALDI-TOF mass spectrum. Four sets of GPC separations were achieved by dividing 63 mg sample, the band (2)' mainly comprised of dimer **11** was GPC chromatographed again, yielding 7.5 mg (6.0 μmol); 0.4% (isolated yield from the band (2)) of dimer **11**. The band (3) afforded analytically pure free base monomer **9** according to ^{1}H-NMR spectra, and yielded 190 mg (285 μmol; 12.7% (isolated yield)).

2.5.5   Free base porphyrins in the second cyclization step

The solvent $CHCl_3$ was treated with nitrogen gas bubbling for more than 5 min.

Starting materials, 1-methyl-2-imidazolecalbaldehyde (9 mg, 83 μmol), and *n*-heptyldipyrromethane 5 (25 mg, 104 μmol) were dissolved in $CHCl_3$ (11 mL) into a 50

mL one-neck round-bottom flask comprising of 5-(3'-formylphenyl)-15,20-bis(*n*-heptyl)-10-imidazolylporphyrin 10 (14 mg, 21 μmol). TFA catalyst (13 μL, 166 μmol)

was added, and the reaction mixture was stirred at room temperature, monitored by silica

gel TLC and MALDI-TOF mass. After stirring for 12 h, DDQ (35 mg, 156 μmol) was

added using 2 mL toluene, and the solution was stirred for further 2 h. The acid catalyst

was neutralized by triethylamine (23 μL, 166 μmol), and the solution was poured onto a

pad of deactivated basic alumina column. $CHCl_3$ as eluent was added until free base

porphyrin components were fully eluted, and eluted solution was rotary evaporated to

dryness as a mixture. The mixture of free base porphyrins was dissolved in a minimum

amount of $CHCl_3$, loaded onto silica gel column ($CHCl_3$, then $CHCl_3$/acetone = 5/1 (v/v)).

Two components were separated with the following composition: (1)

mono(imidazolyl)porphyrins (unreacted 10 and exchange reaction byproducts), and (2)

bis(imidazolyl)porphyrins (mainly dimer 11 and monomer 9), the component (1) was

eluted with $CHCl_3$ only, and the component (2) was eluted with $CHCl_3$/acetone = 5/1

(v/v). The component (2) was rotary evaporated to dryness and yielded 7 mg of bis(imidazolyl)porphyrins. Final separation of the component (2) was achieved by dissolving the mixture in a minimum amount of toluene, and chromatographing the solution on GPC columns. Similarly to the single step route, three bands were observed by an UV lamp (365 nm) irradiation. Three sets of GPC separations were achieved by dividing 7 mg sample, yielding the dimer **11** and monomer **9**, 3.6 mg (2.9 μmol; 13.7 %) and 2.9 mg (4.4 μmol; 10.5%), respectively.

5,15-Bis(*n*-heptyl)-10,20-bis(1-methylimidazol-2-yl)porphyrin (9): ^{1}H NMR (400 MHz, $CDCl_3$, rt) δ 9.48 (β, d, 2H, J = 2.0 Hz), 9.47 (β, d, 2H, J = 2.0 Hz), 8.84 (β, d, 2H, J = 5.2 Hz), 8.82 (β, d, 2H, J = 4.8 Hz), 7.71 (Im, d, 1H, J = 1.6 Hz), 7.69 (Im, d, 1H, J = 1.6 Hz), 7.50 (Im, d, 1H, J = 1.6 Hz), 7.48 (Im, d, 1H, J = 1.2 Hz), 4.96 (CH_2, m, 4H), 3.45 (CH_3, s, 3H), 3.36 (CH_3, s, 3H), 2.51 (CH_2, m, 4H), 1.76 (CH_2, m, 4H), 1.51 (CH_2, m, 4H), 1.32 (CH_2, m, 8H), 0.89 (CH_3, m, 6H), –2.70 (NH, s, 1H), –2.71 (NH, s, 1H). From ^{1}H NMR measurements, the author observed three kinds of atropisomer, and these isomers corresponded to almost the theoretical statistic ratio (i.e. 1:1); MALDI-TOF mass (dithranol) *m/z* obsd 667.43 [M+H]$^+$, calcd exact mass 666.42 ($C_{42}H_{50}N_8$); λ_{abs} (benzene) 419, 515, 552, 593, 652 nm; λ_{em} (benzene) 658, 724 nm.

5-(3-Formylphen-1-yl)-10,20-bis(*n*-heptyl)-15-(1-methylimidazol-2-yl)porphyrin

(10): ^{1}H NMR (400 MHz, CDCl$_3$, rt) δ 10.34 (CHO, s, 0.5H), 10.32 (CHO', s, 0.5H), 9.47 (β, d, 2H, *J* = 4.8 Hz), 9.43 (β, d, 2H, *J* = 4.8 Hz), 8.80 (β, d, 2H, *J* = 4.8 Hz), 8.77 (β, d, 2H, *J* = 4.8 Hz), 8.73 (Ph, s, 0.5H), 8.63 (Ph', s, 0.5H), 8.49 (Ph, d, 0.5H, *J* = 7.6 Hz), 8.39 (Ph, d, 0.5H, *J* = 7.6 Hz), 8.35 (Ph, d, 1H, *J* = 7.6 Hz), 7.95 (Ph, t, 0.5H, *J* = 7.6 Hz), 7.92 (Ph, t, 0.5H, *J* = 7.6 Hz), 7.69 (Im, s, 1H), 7.48 (Im, s, 1H), 4.94 (CH$_2$, t, 4H, *J* = 8.0 Hz), 3.42 (CH$_3$, s, 1.5H), 3.40 (CH$_3$, s, 1.5H), 2.50 (CH$_2$, m, 4H), 1.76 (CH$_2$, m, 4H), 1.49 (CH$_2$, m, 4H), 1.32 (CH$_2$, m, 8H), 0.88 (CH$_3$, m, 6H), −2.66 (NH, s, 2H).

From ^{1}H NMR measurements, the author observed two kinds of atropisomer, and these isomers corresponded to almost the theoretical statistic ratio (i.e. 1:1); MALDI-TOF mass (dithranol) *m/z* obsd 691.45 [M+H]$^+$, calcd exact mass 690.40 (C$_{45}$H$_{50}$N$_6$O).

1,3-Bis[10,20-bis(*n*-heptyl)-15-(1-methylimidazol-2-yl)porphyrin-5-yl]benzene (11):

^{1}H NMR (600 MHz, CDCl$_3$, rt) δ 9.59-9.57 (β, m, 4H), 9.45-9.43 (β, m, 4H), 9.39-9.37 (β, m, 4H), 9.24 (Ph, s, 0.25H), 9.10 (Ph', s, 0.5H), 8.96 (Ph", s, 0.25H), 8.75 (β, m, 4H), 8.68-8.66 (Ph, m, 1H), 8.56 (Ph', d, 1H, *J* = 7.2 Hz), 8.17 (Ph, t, 0.25H, *J* = 7.5 Hz), 8.14 (Ph, t, 0.5H, *J* = 7.5 Hz), 8.12 (Ph, t, 0.25H, *J* = 8.7 Hz), 7.45 (Im, d, 2H, *J* = 4.2 Hz),

7.46 (Im, s, 1H), 7.44 (Im, s, 1H), 4.96 (CH$_2$, m, 8H), 3.43 (CH$_3$, s, 3H), 3.40 (CH$_3$, s, 1.5H), 3.35 (CH$_3$, d, 1.5H, J = 2.4 Hz), 2.51 (CH$_2$, m, 8H), 1.78 (CH$_2$, m, 8H), 1.50 (CH$_2$, m, 8H), 1.32 (CH$_2$, m, 16H), 0.87 (CH$_3$, m, 12H), –2.62 (NH, s, 4H). From ^{1}H NMR measurements, the author observed three kinds of atropisomer, and these isomers corresponded to almost the theoretical statistic ratio (i.e. 1:2:1); MALDI-TOF mass (dithranol) m/z obsd 1247.76 [M+H]$^+$, calcd exact mass 1246.77 (C$_{82}$H$_{94}$N$_{12}$); λ_{abs} (benzene) 415, 431, 517, 552, 596, 652 nm; λ_{em} (benzene) 658, 725 nm.

2.5.6   Dynamic Nuclear Magnetic Resonance Spectroscopy

(CDCl$_2$)$_3$ was used as a solvent. The samples **13** (ca. 3 mg) was transferred to a clean and dry NMR tube, deaerated by nitrogen gas, and sealed by a teflon tape. Deaerating was performed to remove paramagnetic oxygen which would result in an additional line broadening factor. Sealing allowed for standing at high temperature measurements. A series of variable temperature NMR measurements was performed by checking the resolution of instrument at each temperature. The data were divided into three groups corresponding to slow and intermediate exchange, coalescence temperature, and fast exchange. The coalescence temperature T in K was defined as the temperature at which the appearance of the spectrum changes from that of two separate peaks to that of a

single, flat-topped peak. At this temperature $k = \pi \Delta v_0 / 2^{1/2}$. Where k is the rate constant for the exchange in s^{-1}, and Δv_0 is the difference in their resonance frequencies at slow exchange region, $\Delta v_0 = v_A - v_B$. A plot of ln k versus $1/T$ (Eyring plot) affords a value for the activation energy E_a from its slope. Using values of k extending over the variable temperature range, 373–301 K, the value of $\Delta G_{298\,K}^{\ddagger}$ at 298 K was obtained from a plot of ln (k/T) versus $1/T$. From values for E_a and $\Delta G^{\ddagger}$, $\Delta H^{\ddagger}$ and $\Delta S^{\ddagger}$ can be evaluated.

Chapter 3   Formation of Macrocyclic Structure from Zinc(II) Gable Porphyrins

3.1   Zinc(II) Insertion Reaction

Porphyrin macrocycles chelate almost every element in the periodic table, and various methods have been discovered to prepare metalloporphyrins such as the acetate method, the pyridine method, the acetylacetonate method, the phenoxide method, the benzonitrile method, the dimethylformamide method, the metal organyl method, and the metal carbonyl method (Smith, 1975b). The author adopted the acetate method to insert zinc(II) ion to imidazolylporphyrin under mild condition at room temperature (Scheme 3.1). Zinc insertion converted quantitatively free base porphyrins (9 and 11) to the corresponding zinc complexes 12 and 13, respectively.

Scheme 3.1   Zinc(II) insertion reaction by the acetate method

$R = n\text{-}C_7H_{15}$
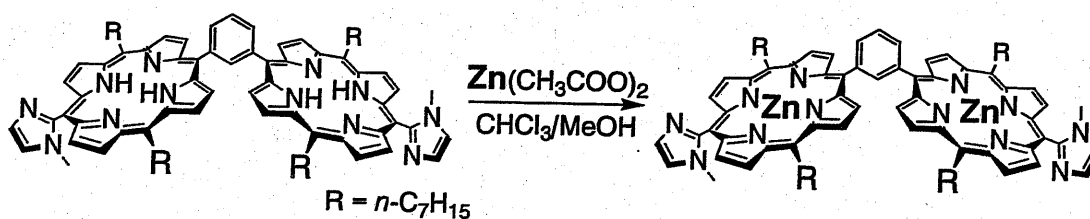
3.2 Reorganization Procedures under High Dilution Conditions

3.2.1 General Statement

Previously, Ogawa and Kobuke have achieved a reorganization of *meso-meso* directly-linked bis(imidazolyl)porphyrin dimer by using coordinating solvents (Ogawa and Kobuke, 2000). This reorganization procedure is comprised of a cleavage and rearrangement processes of self-assembled porphyrin arrays by adding and removing coordinating solvents, respectively. After removing coordinating solvents, the porphyrin arrays express a different arrangement from the original arrays under appropriate conditions. These reorganization processes might be sensitive to the experimental conditions (concentration, ratio of solvents, volume, temperature, and pressure). The author applied the reorganization methods to zinc bis(imidazolyl) gable porphyrin **13**.

3.2.2 Gel Permeation Chromatography

The size distribution of zinc gable porphyrin **13** was analyzed by gel permeation chromatography (GPC) and was observed as a polymeric mixture with broad distributions of the molecular weight (**Figure 3.1**). However, the elution curve was totally different from that of *meso-meso* coupled porphyrin dimer zinc complex, which gave giant linear arrays (Ogawa and Kobuke, 2000). Although the distribution of **13** was

broad, the curve showed obviously longer elution time and distinct peaks at around 12.3

min, indicating the oligomer formation of much smaller molecular weight. This result

suggests that the terminal imidazolyl group tends to find the zinc porphyrin counterpart

at the other chain end leading to intramolecular cyclization rather than zigzag chain

elongation.
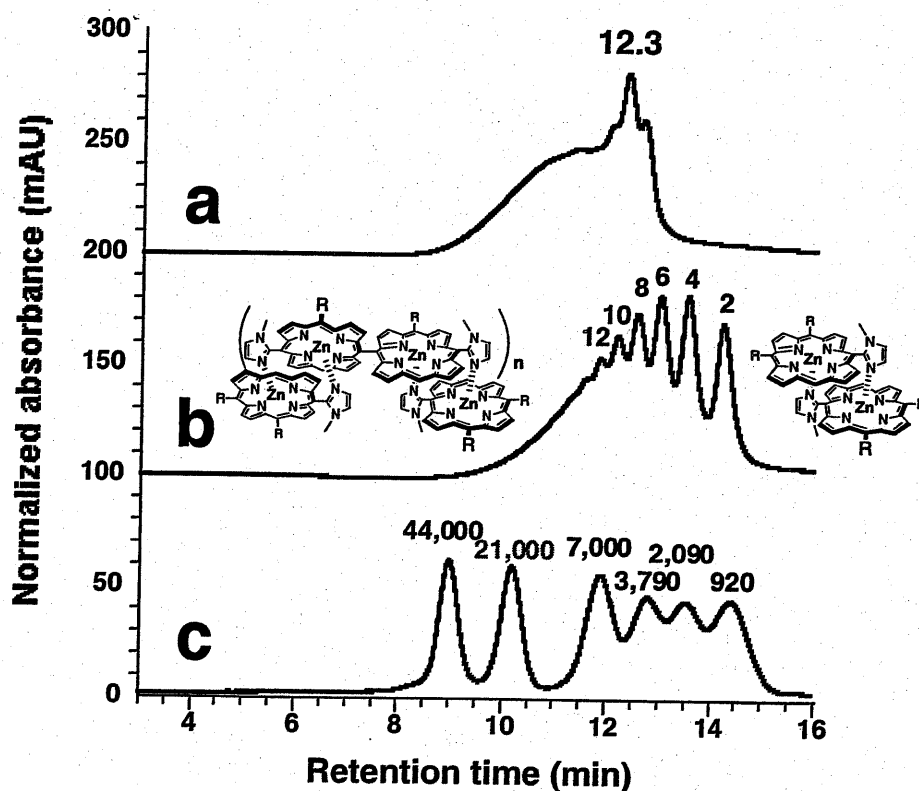
Figure 3.1 Normalized gel permeation chromatograms with a column exclusion volume is 7×10^4 daltons. Each eluent is chloroform. Sequences of (a) **13**, (b) *meso-meso* directly coupled porphyrin oligomer terminated by mono(imidazolyl)porphyrinatozinc(II) monomer. The numbers above each peak correspond to the numbers of porphyrin rings. Inset shows the chemical structure. R = *n*-heptyl group; some *n*-heptyl groups are omitted for clarity. (c) polystyrene standards. The numbers above each peak indicate the molecular weights.

3.2.3   Reorganization under High Dilution Conditions

To dominate the intramolecular cyclization, the author applied the reorganization principle established previously (Ogawa and Kobuke, 2000); coordination bond is formed in non-polar solvents, while broken in polar solvents by competitive coordination, and the process is reversible, but now under high-dilution conditions. The reorganization processes are as follows: (1) Cleavage of the coordinate bond and dilution; **13** was dissolved in 5 μM of $CHCl_3$/methanol = 7/3 (v/v). (2) Further cleavage and dilution; methanol was added to make a 3.5 μM solution of $CHCl_3$/methanol = 1/1 (v/v). (3) Finally, the solvent was evaporated at 25 ± 1 °C. The GPC chart of the sample after the reorganization process showed a dramatic change. In the reorganized sample, **14**, the larger molecular weight part was eliminated almost completely and the peaks were converged to mainly two of the smallest molecular weights (**Figure 3.2**). Considering that cyclic molecules are eluted in general slower than the corresponding linear molecules as shown not only for theoretical consideration (Skvortsov and Gorbunov, 1990), but also for experiment results (e.g. poly(oxyethylene)s (Yu et al., 1996), polycarbazoles (Zhang et al., 1996), and polystyrenes (Lepoittevin et al., 2000)). Therefore the observed molecular weight might be compatible with the closed structure of macroring of gable porphyrins.
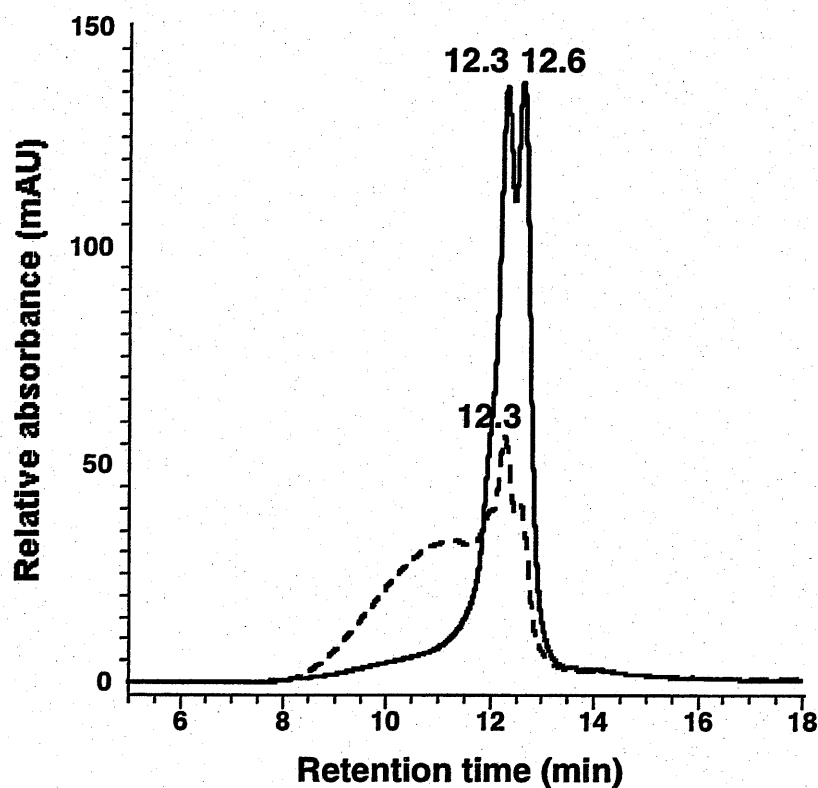
Figure 3.2 Gel permeation chromatograms for **13** (dashed curve) and **14** (solid curve) with a column exclusion volume of 7 × 10⁴ daltons. Each eluent is chloroform and 150 μM solutions were injected.

During the reorganization processes under high diluted conditions, relatively

dissociated oligomers are dominated by the enthalpy term from the large association

constant between slipped-cofacial motives and formed coordinate bonds. Furthermore,

the high dilution conditions preferentially affect rather the formation of the macroring

array than that of the zigzag chain elongation. Meanwhile, in large number of aggregates like after the zinc insertion reaction, the entropy term might be predominated by the enthalpy term and the broad molecular weight distribution was afforded by uncoordinated species. Since such a broad molecular weight distribution was observed in linear porphyrin arrays (Ogawa and Kobuke, 2000), these thermodynamical speculation might be reasonable assessment. It should be noteworthy that the peak at 12.3 min in **Figure 3.2** constantly exists even after the first zinc insertion reaction under concentrated conditions (**Figure 3.1**), and this component must be the most thermodynamically stable molecular assembly. The peak at 12.6 min might be forcedly formed during the reorganization processes under high dilution conditions. Further separation of two components was performed by using size exclusion chromatography, toluene or benzene as eluents (**Figure 3.3**). In the following discussions, the first and the second components are named **15** and **16**, respectively.
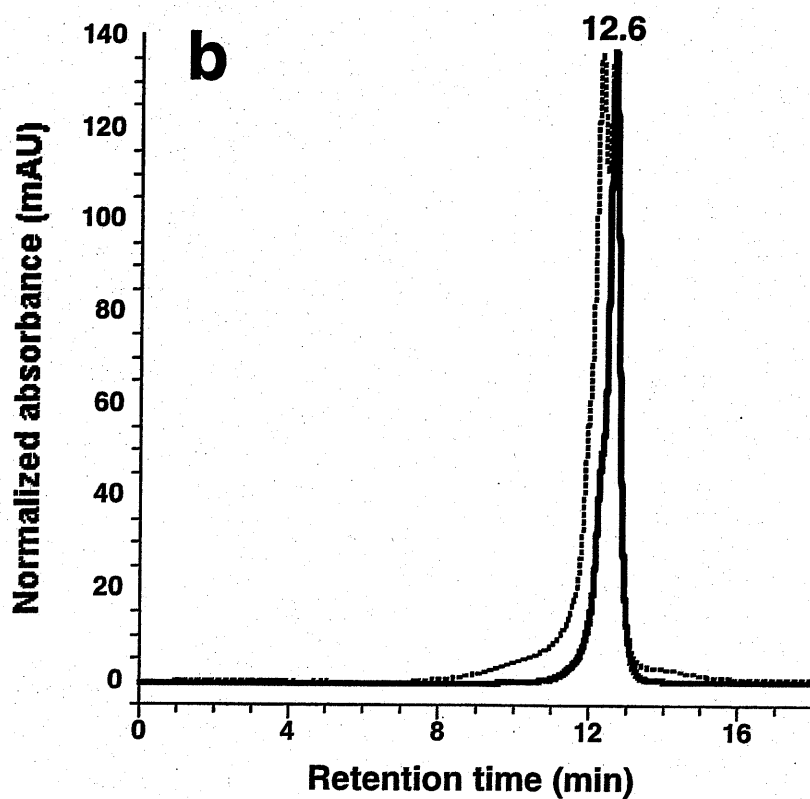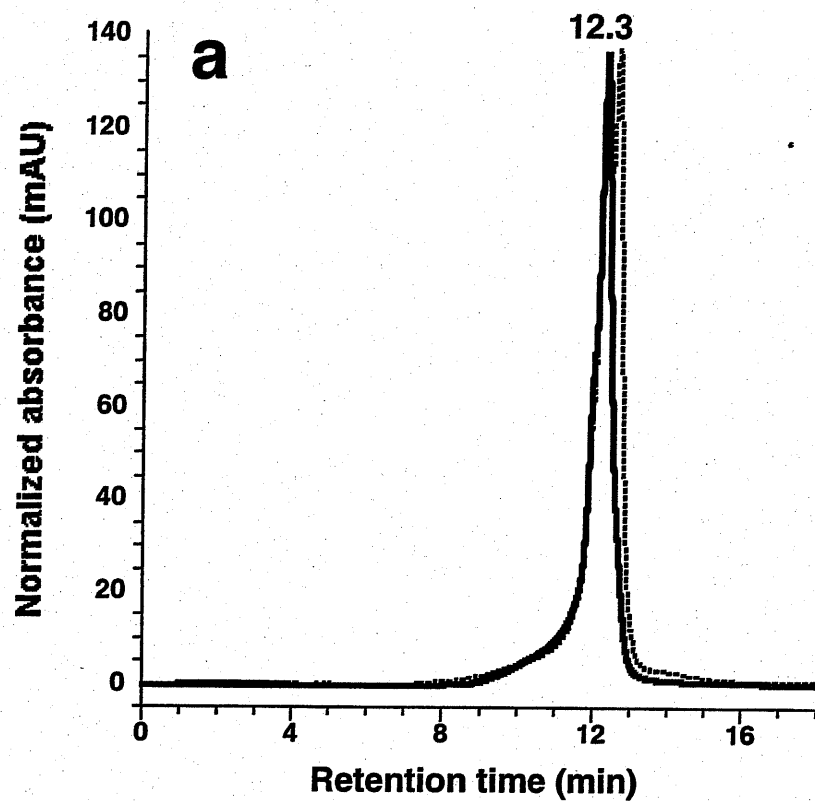
Figure 3.3 Separated two components (a) **15** and (b) **16** by using size exclusion chromatography.

3.3   Probe Microscopy

3.3.1   General Statement

Probe microscopy (Scheuring *et al.*, 2001) and low-temperature single-molecule spectroscopic (van Oijen *et al.*, 1999) techniques have been applied to the natural photosynthetic systems, and individual characteristics have been revealed.

3.3.2   Atomic Force Microscopy

Atomic force microscope (AFM) measurements of **14** on flat mica substrate demonstrated the presence of round-shaped particles (**Figure 3.4**). Further enlargement observation gave round-shaped particles of a uniform height (ca. 1.5 nm) (**Figure 3.5**). The size, after correction of the radius curvature of the AFM probe (ca. 10 nm), provides the net diameter of the particles as a few nm. These particles are main components of the minimum size corresponding to the barrel shaped macroring, although accompanied by larger ones presumably of their aggregates. Therefore the reorganization processes converted completely the polymeric assemblies **13** to a barrel structured mixture **14**. Separation of **14** by preparative GPC afforded finally **15** and **16** as the first and second eluting components, respectively. It should be noted that each component (**15** and **16**) is very stable both in solid states and in solution unless using coordinating solvents. In

AFM measurements, most particles were observed singly and similar particles were also

observed on highly oriented pyrolytic graphite (HOPG) sufaces (**Figure 3.6**). There was

a tendency that particles were observed along with a step of HOPG surface.
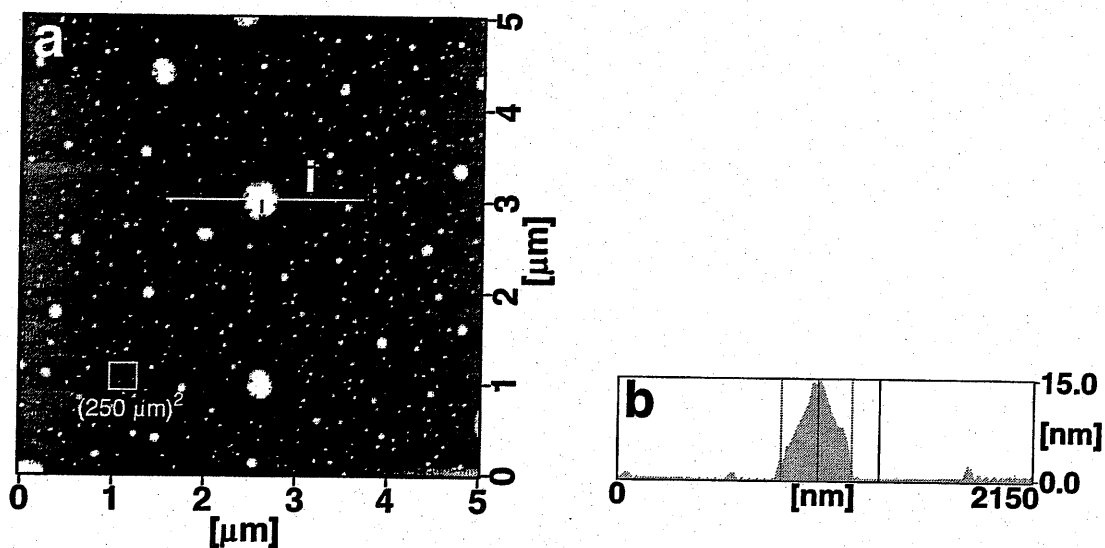
Figure 3.4 Results of AFM measurements. (a) AFM image of **14** spin coated on mica substrate. (b) Cross section profile of particle **i**.

particle	height (nm)	width (nm)
i	1.40	26.8
ii	1.47	25.6
iii	1.39	26.7
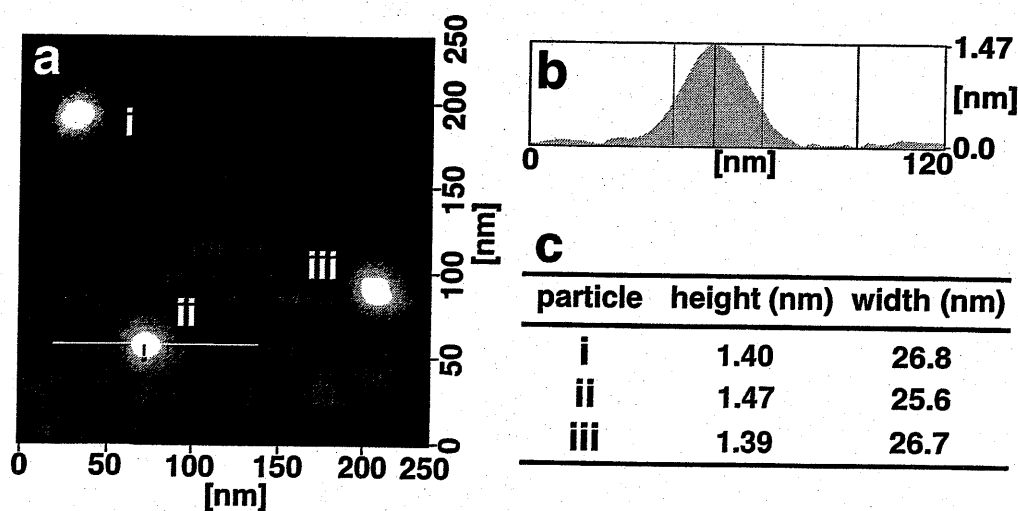
Figure 3.5 Results of AFM measurements. The observed area corresponds to the area framed by square in **Figure 3.4**. (a) AFM image of 14 spin coated on mica substrate. (b) Cross section profile of particle **ii**. (c) Height and width of each particle.
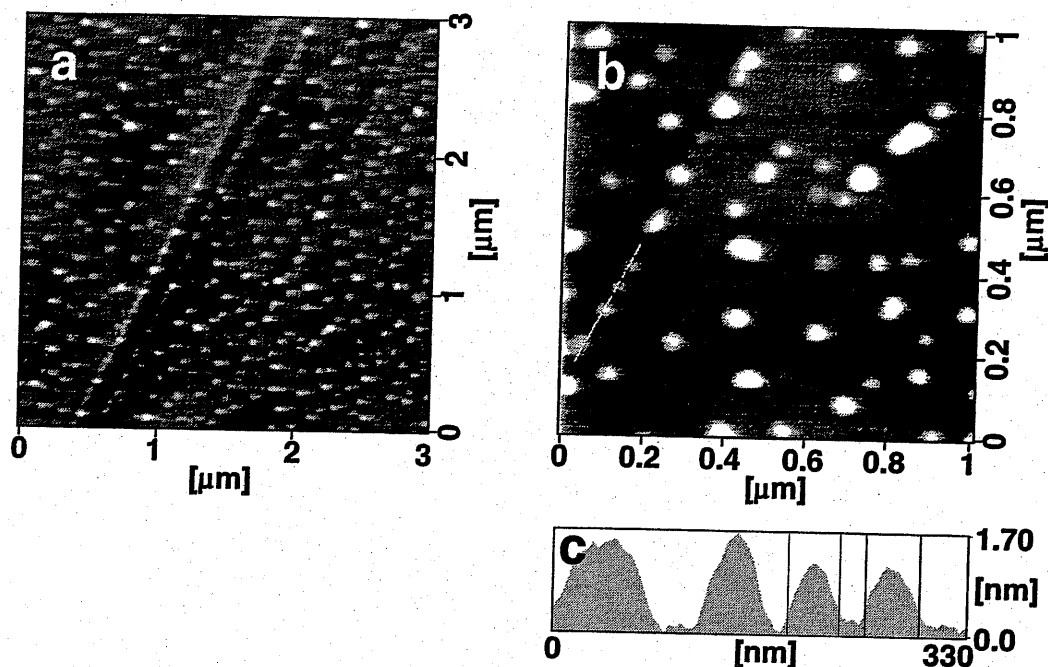
Figure 3.6 Results of AFM measurements. (a) AFM image of **14** spin coated on HOPG substrate. (b) More enlarged image of **14** on HOPG. (c) Cross section profile of particles along with a step of HOPG substrate in (b).

3.3.3 Scanning Tunneling Microscopy

Scanning tunneling microscopy was performed on highly oriented pyrolytic graphite

(HOPG) sufaces, which were preliminary confirmed uniformed particles by AFM

measurements as shown in **Figure 3.6**. Similar to AFM images, many particles tended to

locate along with steps of HOPG surface in STM measurements. However the end group

of n-heptyl substituents seem to interact with HOPG surface, while this group might be

difficult to observe the atomic image by STM probe because of its flexibility. Although

the author could observe only one molecular image of low resolution (**Figure 3.7**), this

image was good in agreement with the size of macroring of gable porphyrins.
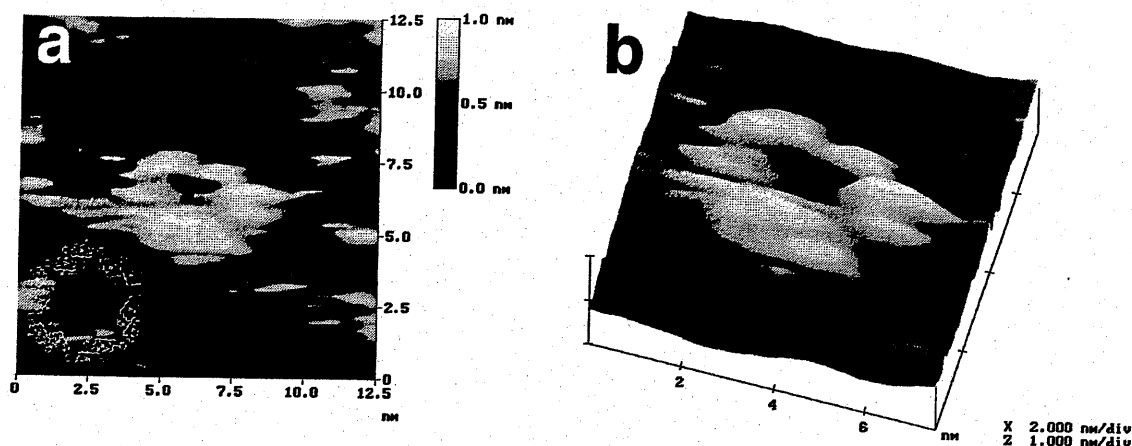
Figure 3.7 Results of STM measurements. (a) STM image of **14** spin coated on HOPG substrate. (b) Birds-eye view of particle **a**.

3.4 Synchrotron Solution Small-angle X-ray Scattering

3.4.1 General Statement

Small-angle X-ray scattering (SAXS) measurement affords: (1) global size from q^2–ln $I(q)$ plot (Guinier plot), (2) molecular shape information from q–ln $I(q)$ plot, and (3) molecular weight from scattering intensity at the origin $I(0)$, where q and $I(q)$ are scattering vector in $Å^{-1}$ and scattering intensity, respectively. To determine the exact aggregation number, the author applied SAXS measurements for **15** and **16** with synchrotron radiation.

3.4.2 Guinier analysis

The results of SAXS measurements for the first component **15** in GPC with synchrotron radiation are as follows. The plot of scattering intensity *vs.* square scattering vector (Guinier analysis) provided a radius of gyration (R_g) 15.59 ± 0.34 Å for the predominant (98.0%) component (**Figure 3.8**). This R_g value corresponds to diameters of 42.36 and 40.26 Å according to sphere and cylinder approximations, respectively. These values agree well with the estimation of ca. 41 Å for the outer diameter of cyclic hexamer from molecular mechanics calculation with a universal force field (UNIVERSAL 1.02) (Rappé *et al.*, 1992). Further, the particle size distribution was evaluated by the Funkuchen analysis, and the remaining 1.99% component gave R_g = 49.05 Å which might correspond to a higher ordered aggregated particles.

Similar to **15**, SAXS measurements of the second component **16** in GPC analysis were performed with synchrotron radiation. The Guinier analysis gave R_g = 11.12 ± 0.66 Å, and this R_g value corresponds to diameters of 28.96 Å according to the cylinder approximation (**Figure 3.8**). Unfortunately, these SAXS results of **16** might be relatively less reliable, because the scattering intensity was relatively low gained.
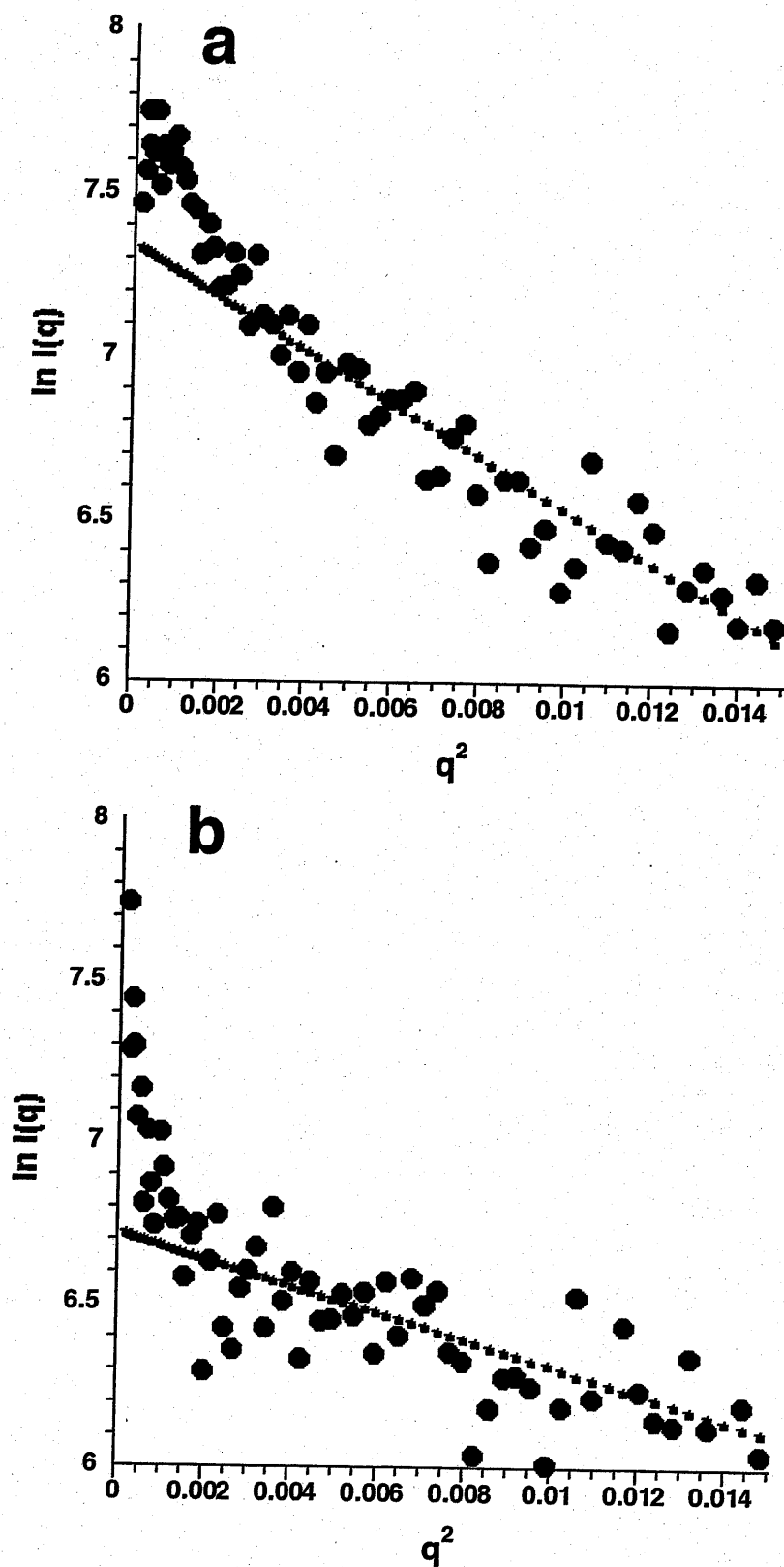
Figure 3.8 The Gunier plot for SAXS measurements of (a) **15** in a methyl benzoate solution (2.2 mg/mL) and (b) **16** in a methyl benzoate solution (2.0 mg/mL). Where q is the scattering vector in $Å^{-1}$ and $I(q)$ is the scattering intensity.

3.4.3 Theoretical Calculation from Model Structures

To confirm the SAXS results, the author compared the experimental results with theoretical calculation results by using molecular mechanics calculations by Cerius[2] with a universal force field (UNIVERSAL 1.02) (Rappé *et al.*, 1992) and a program package for SAXS analysis CRYSOL (Svergun *et al.*, 1995). The representative models are shown in **Figure 3.9** with their theoretical R_g values. However, three kinds of cyclic hexamers were considered with C_2, C_3, and C_6 symmetries in calculation, these isomers have similar R_g values, 16.54, 16.14, and 16.67 Å, respectively, and their distinction might be quite difficult in these experiments. The R_g values for cyclic pentamer and tetramer gave 13.52 and 10.55 Å, respectively. The obtained R_g values for **15** is between cyclic hexamer and cyclic pentamer, and one for **16** is between cyclic pentamer and cyclic tetramer. It should be noted that linear arrays distinctly have larger R_g values than those of corresponding cyclic arrays, 28.34, 23.76, and 19.43 Å for linear-hexamer, pentamer, and tetramer, respectively. Therefore, **15** and **16** must be cyclic arrays in solution by considering with the GPC results. Taking into account of low scattering intensity, **15** and **16** might be corresponding to cyclic hexamer and cyclic pentamer, respectively.
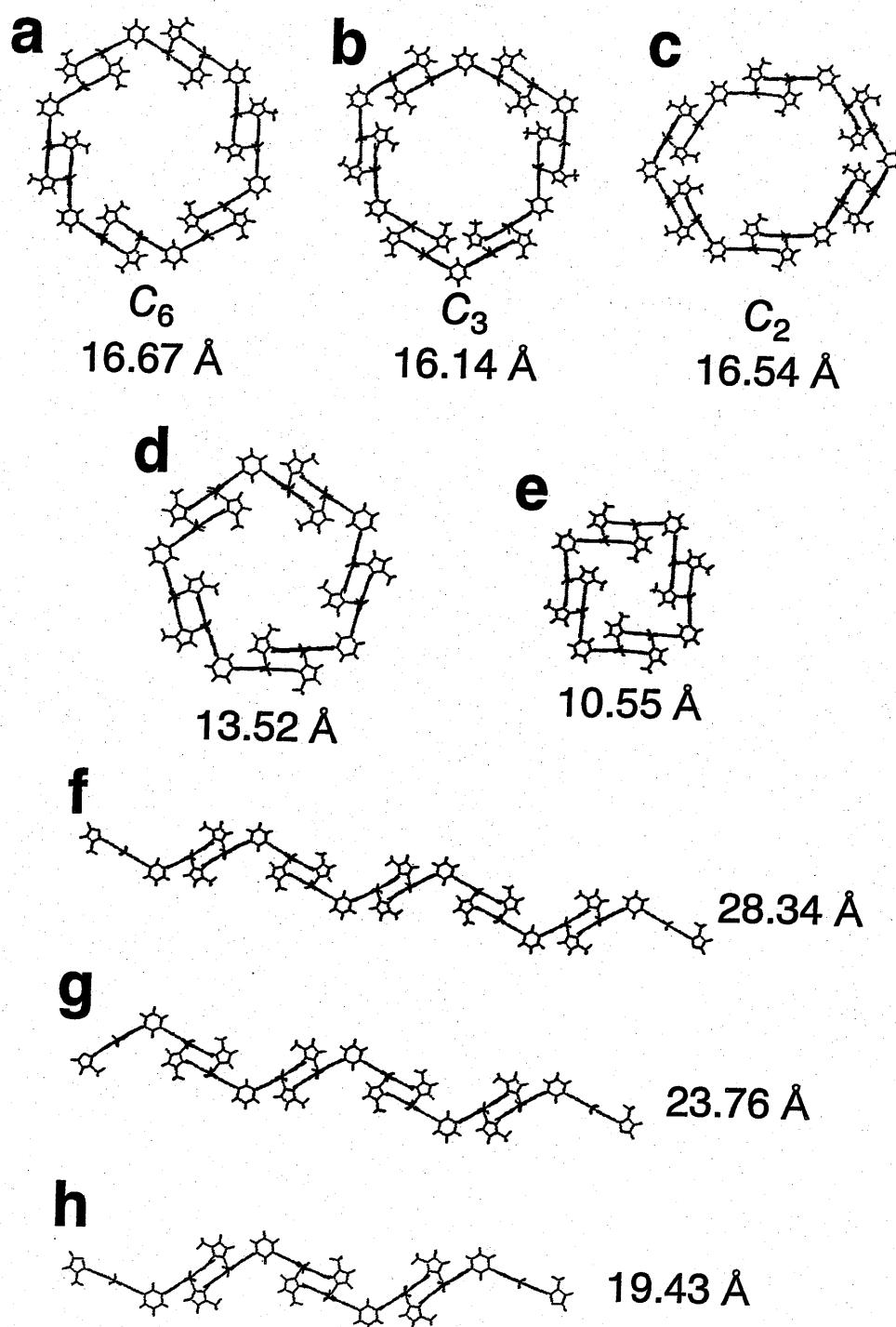
Figure 3.9 Theoretical models and their R_g values. (a) Cyclic hexamer with C_6 symmetry. (b) Cyclic hexamer with C_3 symmetry. (c) Cyclic hexamer with C_2 symmetry. (d) Cyclic pentamer. (e) Cyclic tetramer. (f) Linear hexamer. (g) Linear pentamer. (h) Linear tetramer.

Furthermore, a wide-angle region of the scattering profile was compared between theoretical models. This region reflects molecular shape information from q–ln $I(q)$ plots (Pickover and Engelman, 1982). Theoretical q–ln $I(q)$ plot for the model structures are shown in **Figure 3.10**. The cyclic hexamers with C_6, C_3, and C_2 symmetries have similar scattering profiles and the author could not distinguish between them as same as the R_g values. While distinct difference were observed for cyclic hexamer, cyclic pentamer, and cyclic tetramer, they have waved scattering profiles with the first minimum peaks at 0.18, 0.23, and 0.30 Å^{-1}, respectively. It should be noteworthy that these waved scattering profiles are not observed for linear oligomers, have monotonous profiles. Therefore observed waved profiles for cyclic oligomers might be characteristic for the hollow cylinder structures.
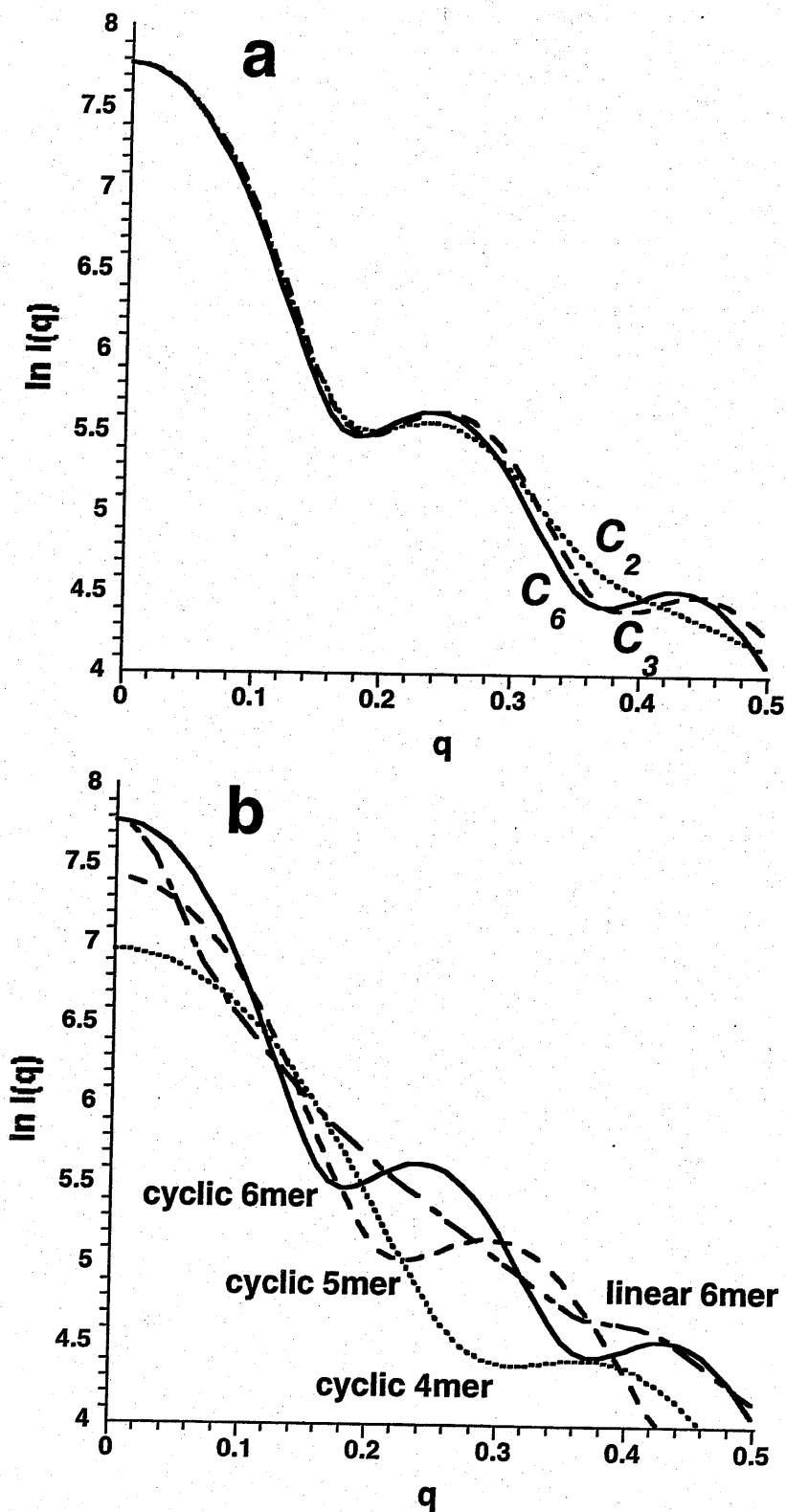
Figure 3.10 Theoretical q–ln $I(q)$ plot for the model structures. (a) The cyclic hexamers with C_6, C_3, and C_2 symmetries are indicated as solid, broken, and dotted lines, respectively. (b) The cyclic hexamer with C_6 symmetry, cyclic pentamer, cyclic tetramer, and linear hexamer are indicated as solid, broken, dotted, and dash-dotted lines, respectively.

3.4.3 Scattering Profiles

In a wide-angle region of the scattering profile, both **15** and **16** gave waved profiles characteristic for the hollow cylinder structure. The first minimum peak of **15** appeared at 0.17 Å^{-1} followed by a rise of the intensity. The scattering intensity plot is expressed by a theoretical calculation (Svergun *et al.*, 1995) best for the cyclic hexamer with a minimum at 0.18 Å^{-1}, in contrast to other cyclic oligomers, the minimum being 0.23 and 0.30 Å^{-1} for a cyclic pentamer and a tetramer, respectively (**Figure 3.11**). The author conclude that **15** is a hexameric macroring. In the case of **16**, however scattering intensity was relatively low gained, the first minimum peak was observed around 0.18–0.26 Å^{-1} (**Figure 3.12**). Because this value roughly corresponds to the cyclic pentamer, the author tentatively assign that **16** is a pentameric macroring.
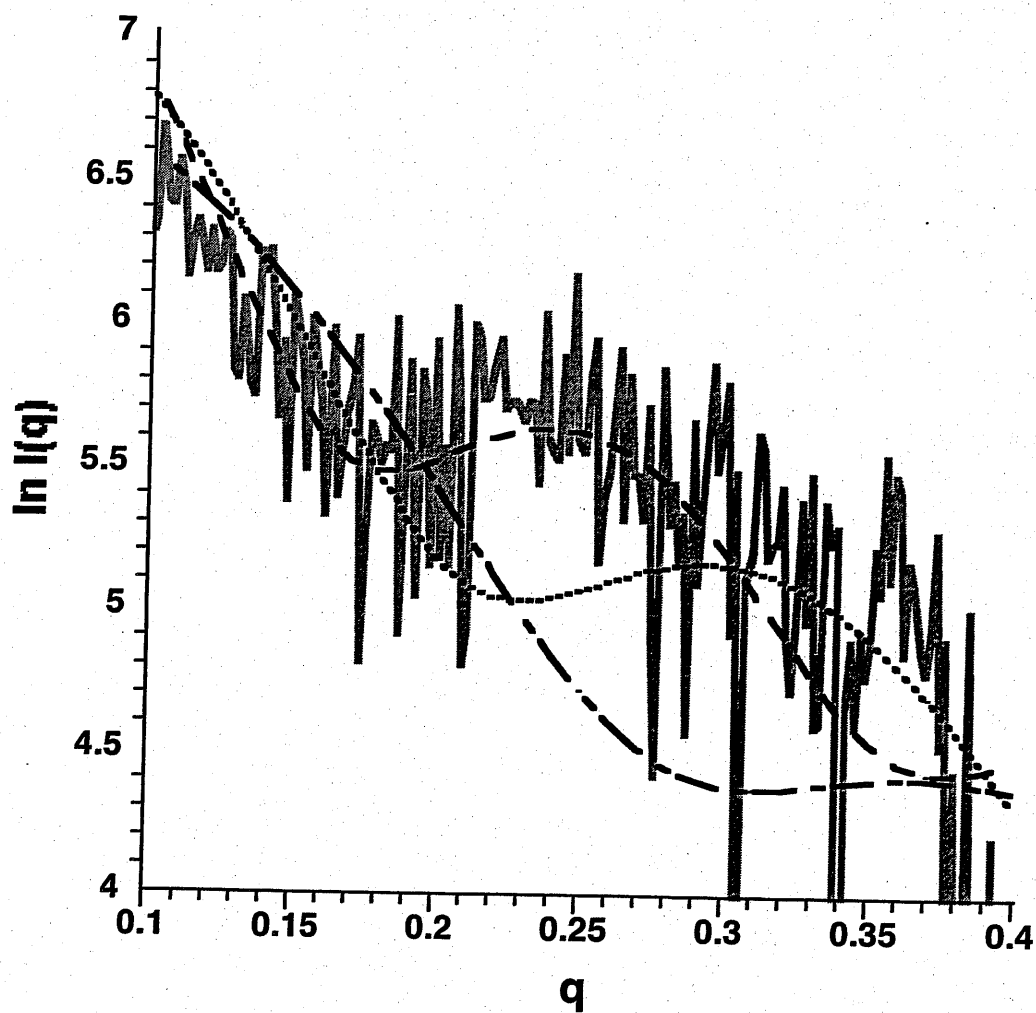
Figure 3.11 q–ln $I(q)$ plot for SAXS measurements of **15** (solid curve) in a methyl benzoate solution (2.2 mg/mL). The theoretical curves for the cyclic hexamer, pentamer, and tetramer are indicated as broken, dotted, and dash-dotted lines, respectively.
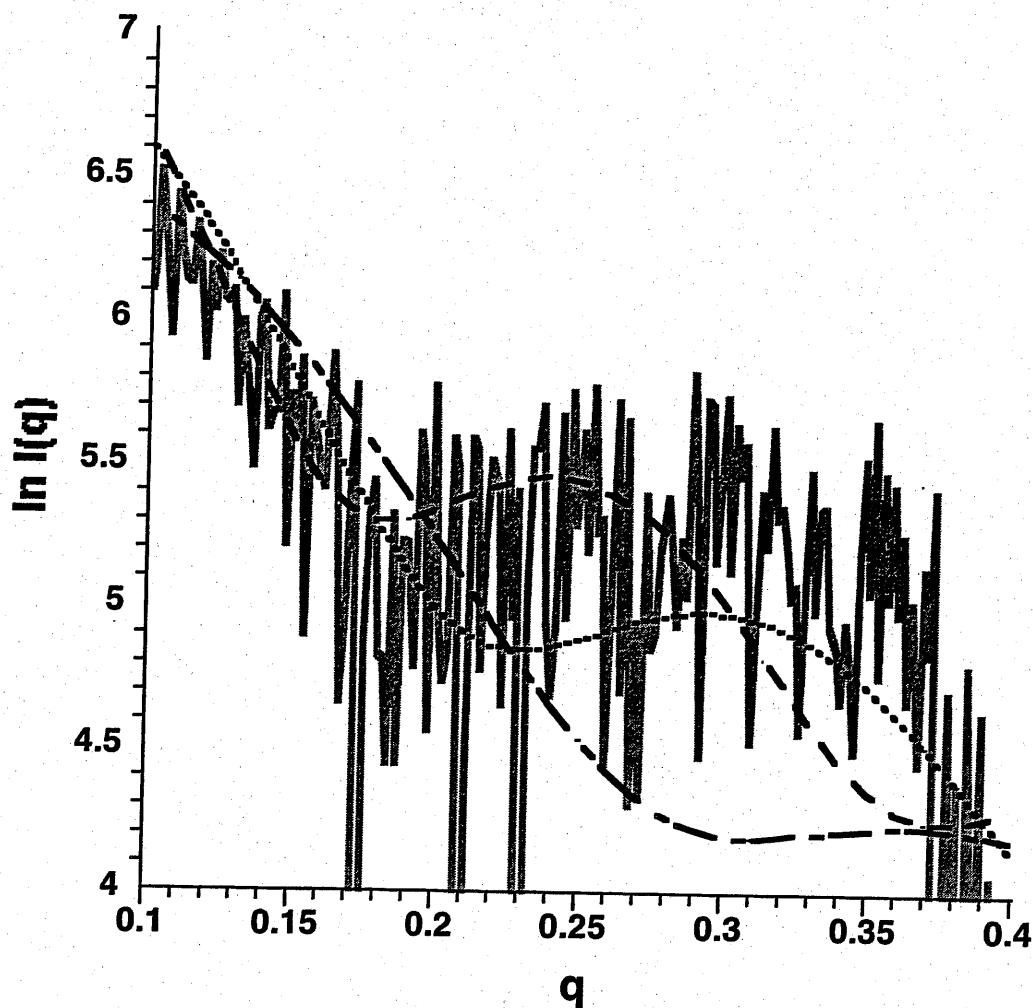
Figure 3.12 q–ln $I(q)$ plot for SAXS measurements of **16** (solid curve) in a methyl benzoate solution (2.0 mg/mL). The theoretical curves for the cyclic hexamer, pentamer, and tetramer are indicated as broken, dotted, and dash-dotted lines, respectively.

3.5   Conclusion

From various measurements, the author conclude that **15** is a hexameric macroring of

gable porphyrins and that **16** is presumably a pentameric macroring of those as shown in

Figure 3.13.
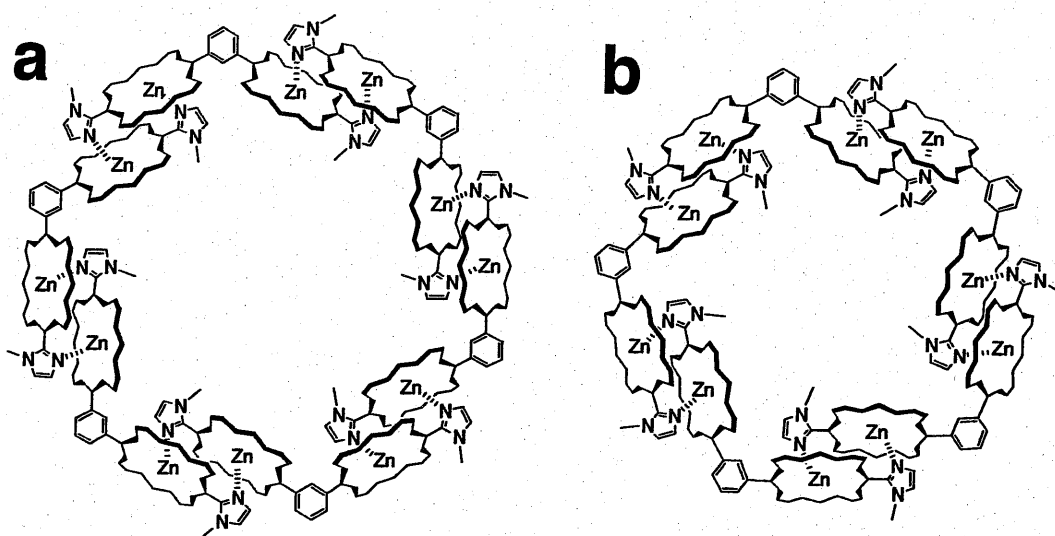
Figure 3.13   Schematic molecular structures of (a) hexameric and (b) pentameric macroring of gable porphyrins.

3.6　Experimental Section

3.6.1　Reagents

All reagents were obtained commercially and used without purification.

3.6.2　Zinc(II) insertion reaction

12: Zinc complex of **9**; A sample of free base porphyrin **9** (4.5 mg, 6.8 μmol) was dissolved in 2 mL of $CHCl_3$ into a 50 mL one-neck round-bottom flask, and then a methanolic solution of $Zn(OAc)_2 \cdot 2H_2O$ (200 μL of methanol) was added. The reaction mixture was stirred at room temperature and monitored by TLC. After 1 h, the reaction mixture was added by ca. 2 mL of $CHCl_3$, and evaporated to remove methanol. The dried reaction mixture was dissolved in 15mL of $CHCl_3$, transferred to a 50 mL separating funnel, the solution was washed with distilled water (10 mL; 5 times), the organic layer was concentrated and dried affording 4.2 mg (5.8 μmol; 85.2%) of a purple solid **12**.

MALDI-TOF mass (dithranol) m/z obsd 729.45 $[M+H]^+$, calcd exact mass 728.33 ($C_{42}H_{48}N_8Zn$); λ_{abs} (chloroform) 412, 435.5, 564.5, 621.5 nm; λ_{em} (chloroform, excitation at 436 nm) 626, 682 nm.

13: Bis-zinc complex of **11**; A sample of free base porphyrin **11** (7.5 mg, 6.0 μmol) was dissolved in 1.5 mL of $CHCl_3$ into a 50 mL one-neck round-bottom flask, and then a methanolic solution of $Zn(OAc)_2 \cdot 2H_2O$ (300 μL of methanol) was added. The reaction mixture was stirred at room temperature and monitored by TLC. After 1 h, the reaction mixture was added by 1 mL of $CHCl_3$, and evaporated to remove methanol. The dried reaction mixture was dissolved in 15mL of $CHCl_3$, transferred to a 100 mL separating funnel, the solution was washed with distilled water (10 mL; 5 times), the organic layer was concentrated and dried affording 7.5 mg (5.5 μmol; 91.7%) of a purple solid **13**. MALDI-TOF mass (dithranol) m/z obsd 1371.57 $[M+H]^+$, calcd exact mass 1370.60 $(C_{82}H_{90}N_{12}Zn_2)$; λ_{abs} (chloroform) 409.5, 446.5, 566.5, 622.5 nm; λ_{em} (chloroform, excitation at 447 nm) 625, 681 nm; λ_{abs} (1-methylimidazole) 425.5, 440.0, 565.0, 618.0 nm; λ_{em} (1-methylimidazole, excitation at 440 nm) 623, 678 nm.

3.6.3   Reorganization procedure under high dilution conditions

The zinc complex **13** (0.2 mg, 0.15 μmol) was transferred to a 50 mL one-neck round-bottom flask dissolving in 30 mL of a $CHCl_3$/methanol = 7/3 (v/v) solution. The solution was added gradually by 12 mL of methanol to yield finally 42 mL of a $CHCl_3$/methanol =

1/1 (v/v) solution. This solution was equipped with a rotary evaporator apparatus, and stirred for 5 min under atmospheric pressure at 25 ± 1 °C, and then evaporated in a period of 25 min under reduced pressure at 25 ± 1 °C. Further drying by a rotary pump afforded **14**, which was dissolved in 1 mL of $CHCl_3$ (150 µM), and analyzed using an analytical GPC apparatus. The GPC chromatogram showed two peaks of narrower distribution compared to **13**. Further separation was accomplished by dissolving **14** in a minimum amount of benzene, and chromatographing the solution on the GPC column. In the GPC operation, the components were monitored using a UV lamp (365 nm) irradiation, and two components were separated with the following composition: (1) the first eluted higher molecular weight component **15**, (2) the second eluted low molecular weight component **16** on the basis of analytical GPC measurements.

14: Reorganized sample of **13**; λ_{abs} (chloroform) 409, 446.5, 568, 621.5 nm; λ_{em} (chloroform, excitation at 446 nm) 625, 680 nm.

15: The first eluted component of **14** in GPC purification; λ_{abs} (chloroform) 409.5, 447.5, 566, 622 nm; λ_{em} (chloroform, excitation at 448 nm) 625, 680 nm.

16: The second eluted component of **14** in GPC purification; λ_{abs} (chloroform) 409, 445.5, 565.5, 621 nm; λ_{em} (chloroform, excitation at 446 nm) 625, 680 nm.

3.6.4   Nuclear Magnetic Resonance Spectroscopy

Deuterated chloroform ($CDCl_3$) containing tetramethylsilane (TMS) as an internal

standard was used. Pyridine-d_5 was used for cleavage of complementary coodinate bond.

3.6.5   Solution Small-angle X-ray Scattering

Solution small-angle X-ray scattering experiments were performed by using

synchrotron radiation at the solution scattering station (SAXES camera) installed at BL-

10C, the Photon Factory, Tsukuba, Japan (Ueki *et al.*, 1985). The wavelength of X-rays

was adjusted to 1.488 Å, calibrated by a bent cylindrical mirror to give a quasi-point

focus. The samples were measured with a specially designed cell with quartz windows.

The sizes were 15 μm thickness, 13.5 mm width, 3 mm height, and 1 mm optical path

length. The measurements were carried out at porphyrin concentrations ranging from 2.0

to 2.2 mg/mL at 25 °C. Methyl benzoate was used as a solvent, because of relatively less

background scattering and no interfering peak. Exposure times for each sample were 30

min, and background scatterings were determined before and after the sample

measurements. X-ray scattering intensities in the small angle region are given as $\ln I (q)$

$= \ln I (0) - (1/3) Rg^2 q^2$ (Guinier equation), where q, $I (0)$, and Rg are the scattering

vector in Å^{-1}, intensity at zero scattering angle, and the radius of gyration, respectively.

The vector q is defined by $q = (2\pi \sin \theta)/\lambda$, where 2θ and λ are the scattering angle and the wavelength of the X-ray, respectively. The Rg values were derived from the slope of its Guinier plot, $\ln I (q)$ versus q^2. The Funkuchen analysis was performed by the following relation, $K_n = kW(R_{gn})R_{gn}^3$, where k and $W(R_{gn})$ are the constant and the weight ratio of n-th particle, respectively.

3.6.6 Theoretical calculation of scattering profiles from model structures

The theoretical scattering curves were calculated from the model structures constructed by using the program package CRYSOL (Svergun *et al.*, 1995) based on the model structures constructed by molecular mechanics calculation. As the model structures, the author calculated cyclic oligomers (hexamers, pentamer, and tetramer), linear oligomers (hexamer, pentamer, and tetramer), and monomer (zinc complex of 11). Although three isomeric structures were possible in the cyclic hexamer with C_2, C_3, and C_6 symmetries, the author could not distinguish them because nearly the same sizes and scattering profiles were calculated for these isomers. In a cylinder approximation, the height of cylinder was fixed on 15.0 Å derived from AFM particle images. For 16, the author tried to improve the S/N ratio by applying solvents of different specific gravities

and high-brightness light-source, but the author could not resolve accurately the size of

16 except that the size was smaller than 15, probably because of the relatively small

particle size.

3.6.7   Molecular mechanics calculation

The construction of molecular models was performed using programs Cerius^2 MatSci

(version 4.2-4.6) developed by Molecular Simulations Inc. with a universal force field

(UNIVERSAL 1.02) (Rappé *et al.*, 1992). *N*-heptyl groups were displaced by methyl

groups to decrease the load of calculation. Because of low precision of the force field,

the author utilized constraints for porphyrin planes and phenylene bridges to avoid a

distortion for estimating the modeling sizes.

Chapter 4   Antenna Function of Zinc(II) Gable Porphyrins

4.1   Absorption Spectra

In general, free base and zinc complex of porphyrins all contain two major absorption

bands. The lower energy transitions are called the Q bands in the visible region, and the

higher energy ones are known as the B bands or commonly called the Soret bands in the

near UV region, and these transitions correspond to $S_0 \rightarrow S_1$ and $S_0 \rightarrow S_2$ transitions,

respectively. These absorption bands are $\pi \rightarrow \pi^*$ transitions, involving the electrons in the

π conjugated system of the porphyrin macrocycle (Figure 4.1).
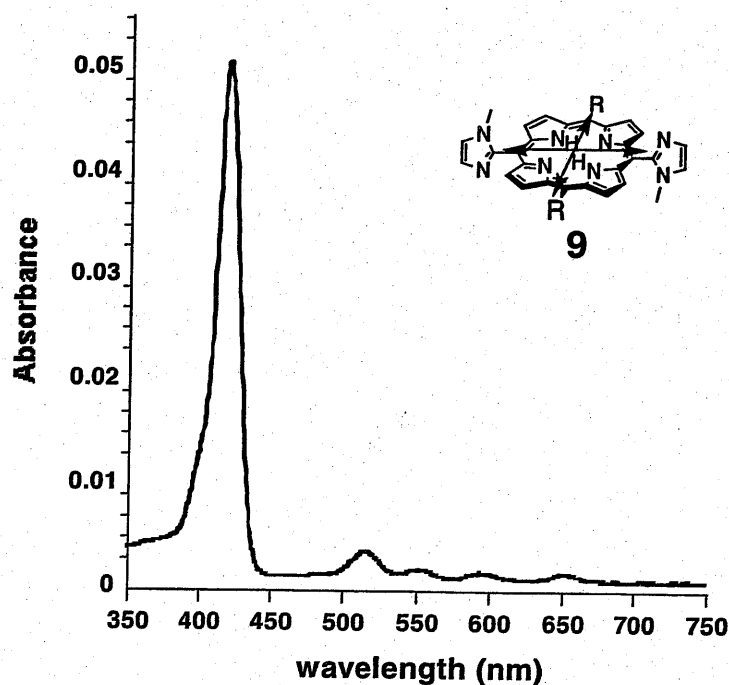
Figure 4.1   UV–vis absorption spectra of monomeric bis(imidazolyl)porphyrin **9** in benzene at room temperature.

Bringing close the distances between chromophores causes a spectral change compared to the monomeric chromophore. This interaction causes shift of the energy levels of chromophores accomplished with redistribution of the oscillator strengths. The Soret or B transitions in symmetrically substituted porphyrins consists of two perpendiculary oriented transitions B_x and B_y; the more intense electronic transition moment, B_x, is in the NH–NH direction at ~420 nm, while a weaker transition moment, B_y, is in the N–N direction at ~400 nm (**Figure 4.1**). Since the NH–NH and N–N groups interchange, and the influence of the symmetry of the *trans*-substituted C_2 porphyrins is unknown, the direction of the B transitions is unsettled. Indeed, in view of the C_2 symmetry of the porphyrin chromophore, in the present case, it may be allowed to define that the electronic transition moment in series of imidazolylporphyrins runs in the *meso-meso* direction. In fact, UV–vis absorption spectra of proximal porphyrins caused a splitting of the Soret band region for both slipped-cofacial and phenylene-bridged motifs (**Figure 4.2**, and **4.3**, respectively).

a

b

Monomer   **Slipped-cofacial motif**
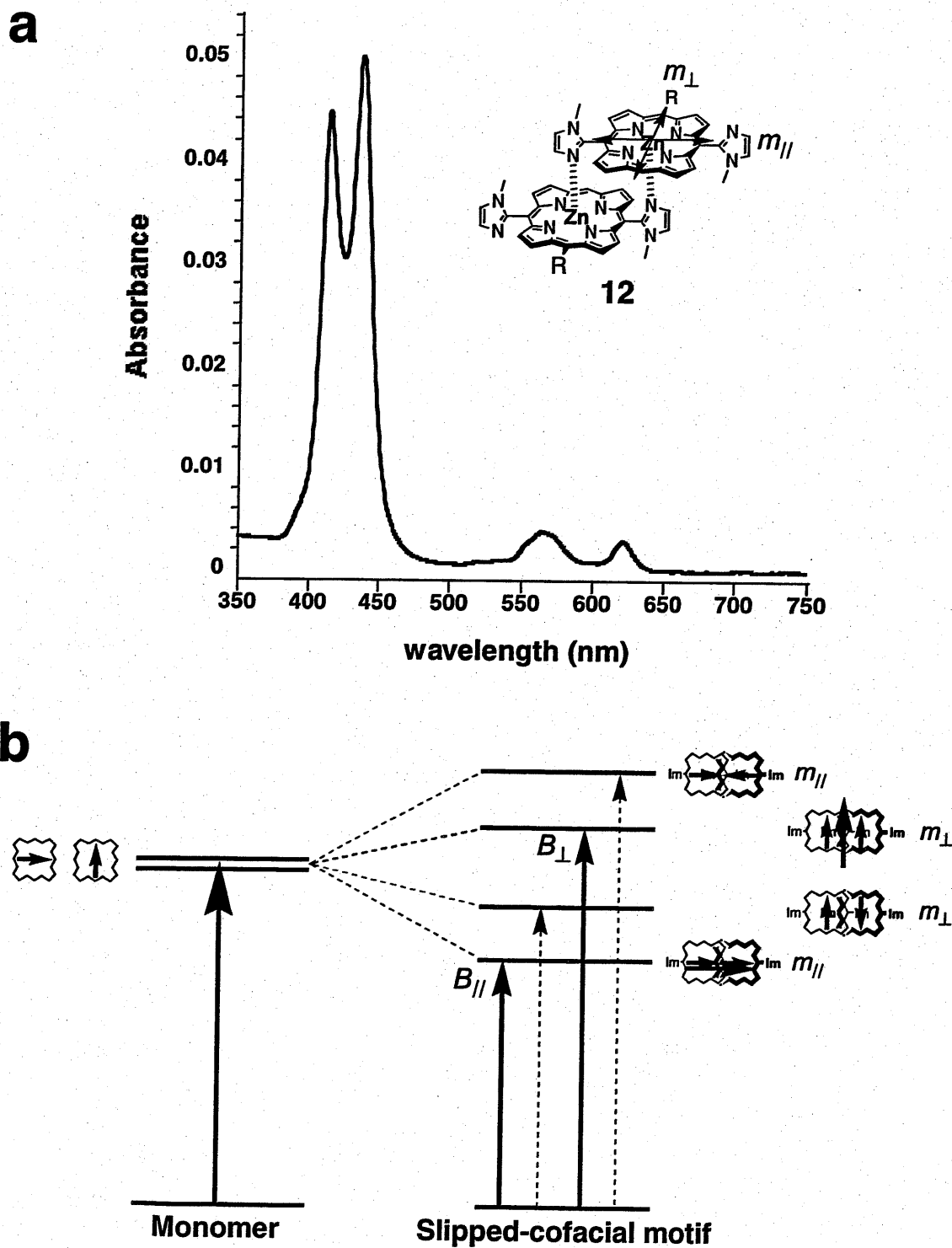
Figure 4.2 (a) UV–vis absorption spectra of the slipped-cofacial motif **12** in benzene at room temperature. (b) Schematic diagram of splitting of the Soret bands.

Figure 4.3 (a) UV–vis absorption spectra of the phenylene-bridged motif **11** in benzene at room temperature. (b) Schematic diagram of splitting of the Soret bands.
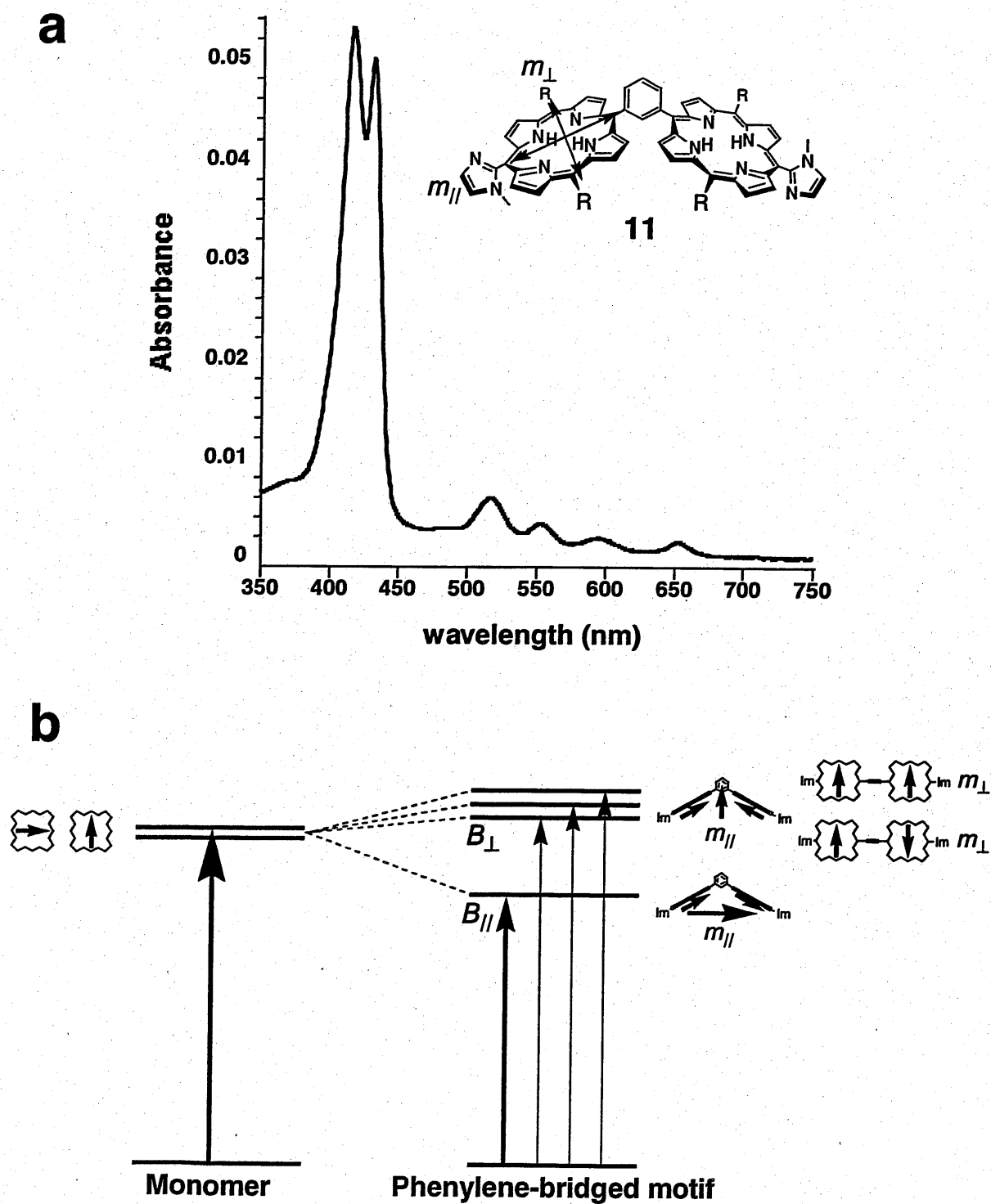
In the case of slipped-cofacial motif, the splitting of the Soret bands might be qualitatively explained by the exciton coupling theory (Kasha *et al.*, 1965). When this theory is applied to the slipped-cofacial arrangement, the degenerated Soret transitions, $B_{//}$ and $B_{\perp}$, in the monomeric unit are red- and blue-shifted depending on the head-to-tail and face-to-face orientations of the transition dipoles $m_{//}$ and $m_{\perp}$, respectively (**Figure 4.2**). In the case of phenylene-bridged motif, the splitting of the Soret bands might be explained similarly. The red-shifted Soret transition $B_{//}$ might be come from the interaction between the transition dipoles $m_{//}$ on the head-to-tail orientation, and the other unperturbed Soret transition $B_{\perp}$ in the monomeric unit might be derived from both the head-to-head (tail-to-tail) orientations of the transition dipoles $m_{//}$ and the unperturbed transition dipoles $m_{\perp}$ (**Figure 4.3**).

UV–vis absorption spectrum of the macroring **14** (hexamer:pentamer ≈ 1:1) solution

gave further large splitting of the Soret bands and relatively unaffected Q bands

compared to the slipped-cofacial dimer **12** (Figure 4.4).
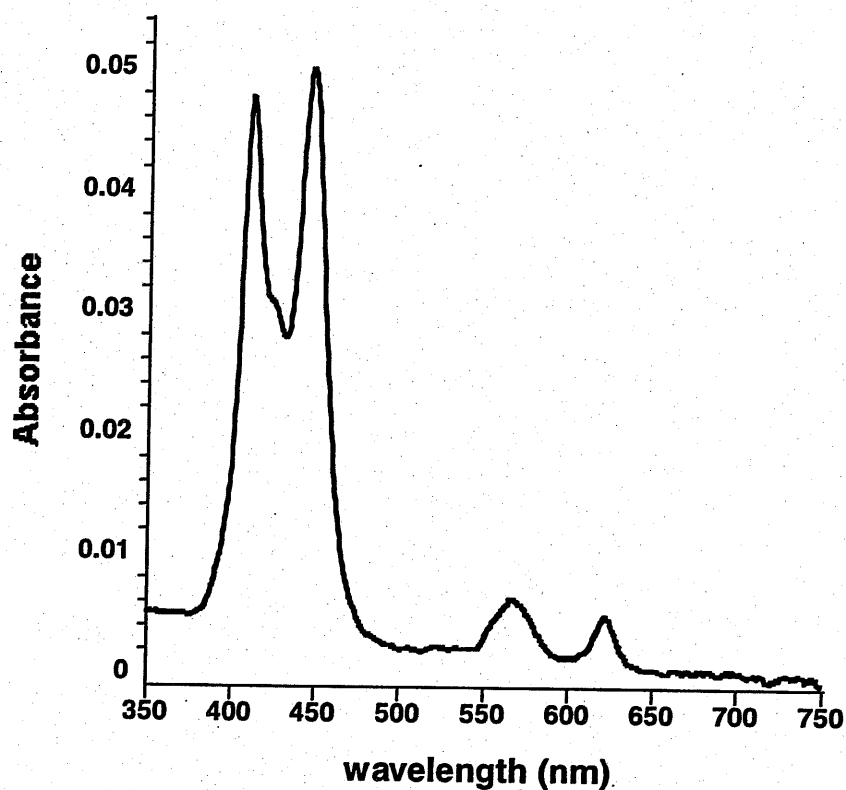
Figure 4.4   UV–vis absorption spectra of the macroring **14** in benzene at room temperature.

These qualitative analysis of the absorption spectra indicates that although electronic

interactions between the closed porphyrins lead to perturbation of the Soret bands, the Q

band absorptions of all porphyrins are negligibly affected when the pigments are linked

to form the array. In the point-dipole approximation, the exciton coupling theory indicates that the interaction between chromophores should be inversely proportional to the cube of the interchromophoric distance and proportional to the square of the transition moments of the interacting chromophores. Thus, long-range exciton coupling in the porphyrin arrays should only be seen for the higher oscillator strength Soret bands and not for the weaker Q bands, as is observed (Osuka and Maruyama, 1988). Similar trends were also observed in chloroform solution, and UV–vis absorption spectrum of the hexamer 15 and the pentamer 16 gave large splits of the Soret bands, 2073 and 2003 cm^{-1}, respectively, these correspond to the sum of each contribution of the splitting energy from slipped-cofacial and phenylene-bridged interactions (Kasha et al., 1965), 1310 and 775 cm^{-1}, respectively, the values of dimer 12 (zinc complex of 9) and of the monomeric bis-zinc gable-porphyrin (measured in 1-methylimidazole).

4.2 Fluorescence Spectra and Photochemical Parameters

Fluorescence emission spectra of the macrorings (14, 15, and 16) are similar to the one of the slipped-cofacial dimer 12 (Figure 4.5), reflecting unperturbed Q bands absorption. These fluorescence spectral peaks of series of zinc porphyrins appear at slightly longer wavelengths than the absorption maximum, and have a characteristic

mirror image relationship to the absorption spectra. This relationship may come from the expectation that the ground- and excited-states have similar shapes, and therefore that the molecular vibrations that are activated during electronic absorption are also likely to be activated upon fluorescence emission. However, in this case, the initial state is the ground vibrational state of the excited electronic state, and the final state is the excited vibrational state of the ground electronic state. This causes a shift of the emission to the longer wavelength side of the main transition, so called the Stokes shift.

Interestingly, while a red-shifted and strongly quenched fluorescence was observed for artificial cofacial zinc dimers (Sanders *et al.*, 1988), imidazolylporphyrin has intense fluorescence emission. After the macroring formation, the macroring **14** also possessed fluorescence emission property, compared to tetraphenylporphyrinatozinc(II) (ZnTPP) **17** as a reference (Seybold and Gouterman, 1969) (**Figure 4.5** and **Table 4.1**). Furthermore, the relative fluorescence quantum yield of hexamer **15** to that of the monomeric bis-zinc gable porphyrin was 0.51 (excited at the longer wavelength band of the Soret bands, respectively). Similar relations have been observed between the natural light harvesting complex and its dimeric subunit constituent (Chang *et al.*, 1990). Detailed studies on photophysics of the porphyrin macroring **15** will be of profound interest in the viewpoint elucidating the relation between structure and function.
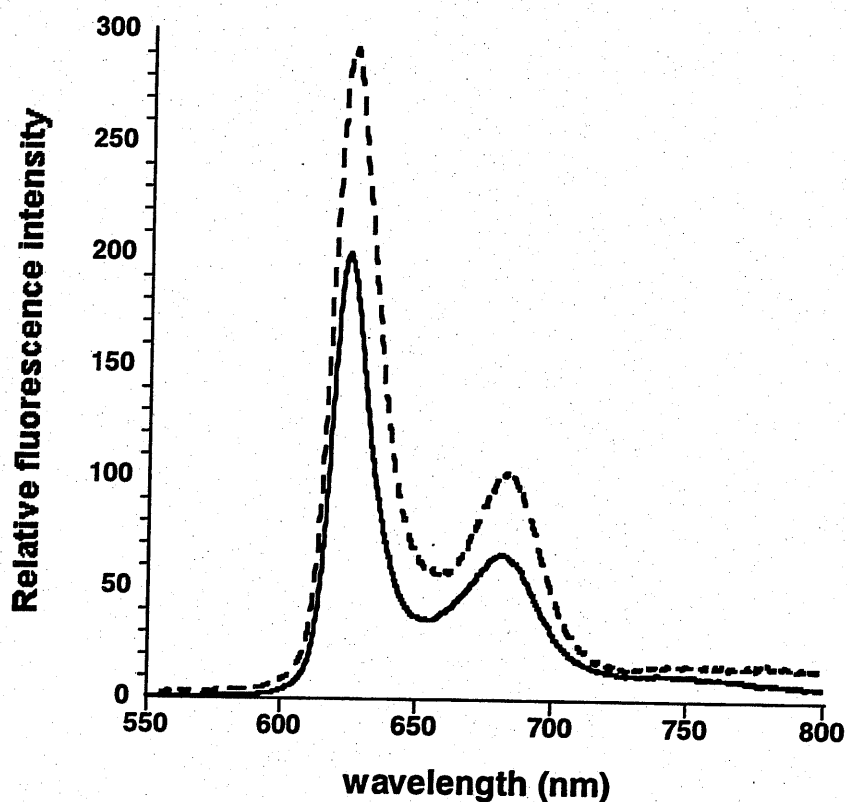
Figure 4.5 Fluorescence emission spectra of the slipped-cofacial dimer **12** (dashed line) and the macroring **14** (solid line) in benzene at room temperature.

Natural radiative lifetimes of the macroring **14** and ZnTPP **17** were calculated using the relation $\tau_M^0 = \tau_M / \Phi_{FM}$, where τ_M^0, τ_M, and Φ_{FM} are the radiative lifetime, the fluorescence lifetime, and the relative fluorescence quantum yield, respectively (**Table 4.1**). In these calculations, the lifetime of excited state porphyrin τ_M was fixed at 2.0 ns

both ZnTPP **17** (Yang *et al.*, 1999) and the macroring **14** (Ikeda *et al.*, 2002).

The author derived the further photophysical parameters according to Longo's approach (Quimby and Longo, 1975). For many aromatic molecules, the sum of the quantum yields of fluorescence and triplet formation is close to 1.0 (Medinger and Wilkinson, 1965). This implies the $k_{TM} \gg k_{GM}$ for those aromatic molecules, where k_{TM} and k_{GM} are the rate constants of intersystem crossing and internal conversion, respectively. Solov'ev *et al.* reported the triplet quantum yields of tetraphenylporphyrin (TPP) to be 0.83–0.87 (Solov'ev *et al.*, 1972). Since the fluorescence quantum yield of TPP is 0.11 (Seybold and Gouterman, 1969), one might assume $k_{TM} \gg k_{GM}$ for TPP and also for the zinc(II) derivatives. The relative rates of intersystem crossing of the macroring **14** and ZnTPP **17** were derived by using the relation $k_M^0 = 1/\tau_M^0$ and $k_{TM} = k_M^0$ $(1 - \Phi_{FM})/\Phi_{FM}$ (**Table 4.1**).

Table 4.1 Photochemical parameters

	Φ_{FM}	τ_M^0 (ns)	$10^6 k_M^0$ (s)	$10^6 k_{TM}$ (s^{-1})
ZnTPP **17**	0.030[a]	66.7	15.0	485
macroring **14**	0.035	57.1	17.5	483

[a] Seybold and Gouterman, 1969

4.3   Fluorescence Quenching Experiment

4.3.1   General Statement

The quenching process of fluorescence has been studied over the last century, and several empirical and theoretical relations have been proposed to describe the observed behavior. In this section, the author will describe the photophysical antenna function of the macroring of gable porphyrins. Detailed photochemical processes are defined in **Appendix**.

4.3.2   Stern-Volmer Analysis

Fluorescence quenching experiments were performed by 1,4-benzoquinone (BQ) as an electron transfer quencher. When a quenching reaction occurs under diffusion-controlled process, the Stern-Volmer relation is derived from (A.14) in the following **Appendix**

$$\Phi_{FM}/(\Phi_{FM})_0 = 1/(1 + \tau_M k_q[BQ]) \qquad (4.3.1)$$

where [BQ] denotes the molar concentration of BQ. And in general, $\Phi_{FM}/(\Phi_{FM})_0 \approx I_0/I$ and $K_{SV} = \tau_M k_q$, where I_0 and I denote the porphyrin emission intensity in the absence and presence of BQ, respectively, and K_{SV} denotes the Stern-Volmer coefficient, and hence

$$I_0/I = 1 + K_{SV}[BQ] \qquad (4.3.2)$$

The Stern-Volmer ([BQ] – I_0/I) plot of porphyrin fluorescence emission quenching by

BQ gave straight lines with segment at y-axis equals unity, both for the solution of the macroring porphyrins **14** (approximately 1:1 mixture of hexameric and pentameric gable porphyrins) and for the solution of a reference of ZnTPP **17** (**Figure 4.6**). The values of I_0 and I were integrated from 580 to 800 nm (i.e. 17.24–12.50 kcm^{-1}) for macroring **14** and from 560 to 800 nm (i.e. 17.86–12.50 kcm^{-1}) for ZnTPP **17**, in the absence and presence of BQ, respectively. The linear relationship of the Stern-Volmer plot observed for the plotted region suggests that any charge transfer and/or excimer complexes did not form during the measurements. Further addition of BQ to the porphyrin **14** solution, the plot of macroring **14** caused a departure from Stern-Volmer relation, indicates a porphyrin-quencher complexation. The Stern-Volmer constant K_{SV} is derived from the slope of the Stern-Volmer plot and 286.57, 39.64 M^{-1} for the macroring **14** and ZnTPP **17**, respectively. The ratio of K_{SV} values from **14** to **17** was 7.23. It should be noted that, while a large molecule has a chance to encounter a quencher molecule easily, a large molecule diffusing more slowly than a small molecule. Therefore, the molecular size effect was roughly canceled in diffusion-controlled quenching processes. However the obtained K_{SV} ratio 7.23 was quite large, and this result indicates an energy migration within the macroring **14** during its excited state lifetime. Similar to the Section **4.2**, throughout following evaluations, the lifetime of excited state porphyrin τ_M was fixed at

2.0 ns both ZnTPP **17** (Yang *et al.*, 1999) and the macroring **14** (Ikeda *et al.*, 2002). By

these assumption that τ_M = 2.0 ns, the experimental k_q values were 1.43×10^{11} and $1.98 \times$

10^{10} M^{-1} s^{-1} for the macroring **14** and ZnTPP **17**, respectively.
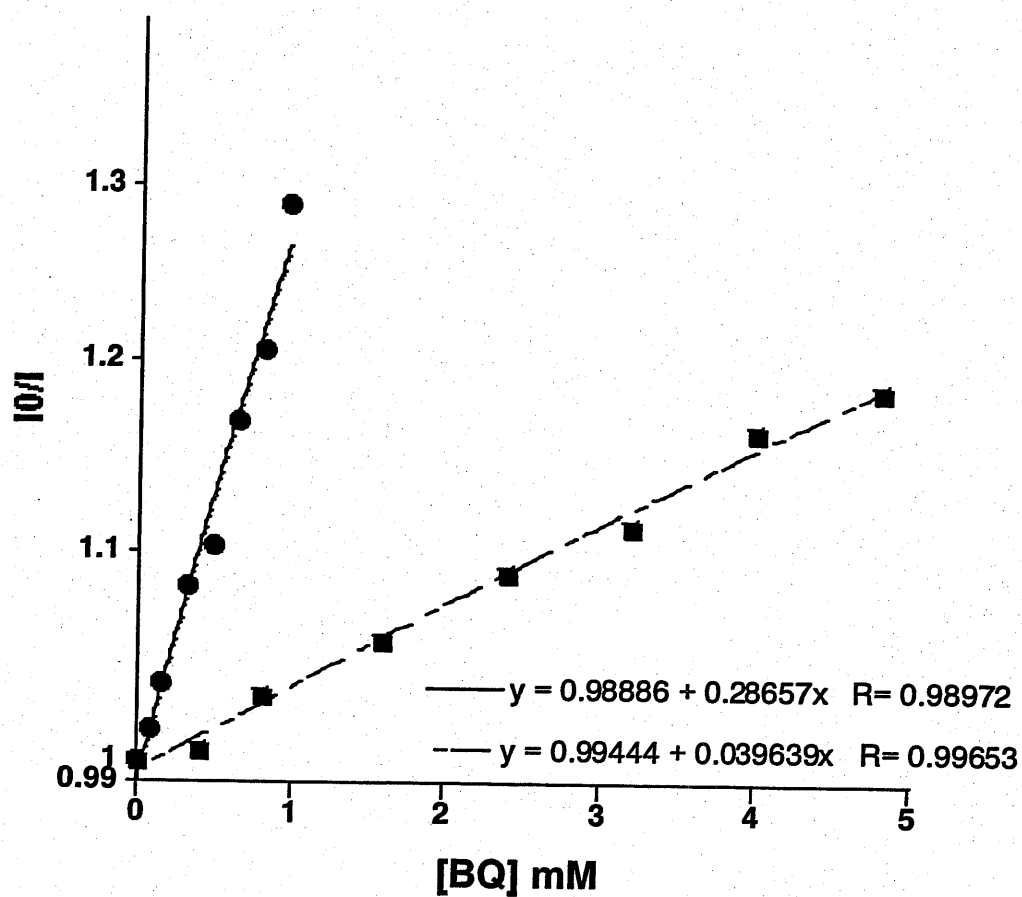
Figure 4.6   Stern–Volmer plot for the macroring **14** (circle) and for ZnTPP **17** (square)
both in aerated chloroform solution at 25.00 ± 0.05 °C.

4.3.3 Diffusion-controlled Process

Again theoretically, $K_{SV} = k_{QM}\tau_M$, where k_{QM} and τ_M denote the second-order rate constant of excited porphyrin quenching by BQ and the lifetime of the excited state of porphyrin, respectively. The quenching reaction in solution in general is considered as a diffusion-controlled collisional process. From the Einstein-Smoluchowski diffusion theory, the rate constant k_{QM} of the diffusion-controlled collision process between the porphyrin and BQ is given as

$$k_{QM} = 4\pi N'Dpa(1 + pa(\pi D\tau_M)^{-1/2})\ (M^{-1}s^{-1}) \qquad (4.3.3)$$

where N' is Avogadro's number N_A divided by 1000, $D = D_P + D_Q$ is the sum of the diffusion coefficient of the porphyrin D_P and that of BQ D_Q, p (≤ 1) is a factor introduced to the quenching probability per molecular collision, and $a = a_P + a_Q$ is the sum of their interaction radii of porphyrin a_P and that of BQ a_Q. The second term in the parentheses $pa(\pi D\tau_M)^{-1/2}$ means a transient component of dynamic quenching and this term can be neglected under the present experimental conditions, where neither $D_P + D_Q$ nor τ_M is very small. Therefore the term in the parentheses in equation (4.3.3) is normally of the order of unity, and it is commonly omitted, so that

$$k_{QM} = 4\pi N'Dpa\ (M^{-1}s^{-1}) \qquad (4.3.4)$$

and may be rewritten by

$$k_{QM} = 4\pi N'(D_P + D_Q)\, p(a_P + a_Q) \quad (M^{-1}s^{-1}) \qquad (4.3.5)$$

In applying the relation (4.3.5) to the quenching rate constant k_{QM}, the author may make the following assumptions in a narrow sense: (1) the microscopic viscosity equals to the macroscopic solvent viscosity η, (2) Stokes' law is applicable to the diffusion of porphyrin and BQ, and (3) Stokes' radii of porphyrin and BQ correspond to b_P and b_Q, respectively. On these assumptions, the Stokes-Einstein relation is valid and the author obtain

$$D_P = k_B T/(6\pi\eta b_P) \text{ and } D_Q = k_B T/(6\pi\eta b_Q) \quad (cm^{-1}s^{-1})(4.3.6)$$

where k_B is the Boltzmann constant, then (4.3.6) becomes

$$k_{QM} = 2RT\, p(a_P + a_Q)(1/b_P + 1/b_Q)/(3000\,\eta) \qquad (4.3.7)$$

where $R = k_B N_A = 1000 k_B N'$ and this equation is reduced to the familiar form

$$k_{QM} = 8RT\, p/(3000\,\eta) \qquad (4.3.8)$$

for a collisional process, in which $a_P = a_Q = b_P = b_Q$.

Under steady state experiments, the transient term being neglected in (4.3.3), the rate constant for the quenching process involving both molecular diffusion and long-range electron transfer is given as

$$k_{QM} = 4\pi N'(D_M + D_Q + \Lambda)pR \qquad (4.3.9)$$

where Λ is the energy migration coefficient having the same dimension as the diffusion

coefficients (cm²/s). These approaches for the estimation of energy migration process are common for the polymer chemistry. In general, there is an assumption that the diffusion coefficient of polymer D_M is negligible and putting $D_M = 0$. In the author's case, each compound can be estimated from its structural parameters. Towards rigorous analyses, the author put structural parameters to each molecule, and van der Waals radii were estimated from van der Waals volumes by spherical approximation (**Table 4.2**). It should be noteworthy that the difference of diffusion constants are negligible between the macroring **14**, isolated hexamer **15**, and isolated pentamer **16**.

Table 4.2 Theoretical diffusion constants D in $cm^2 s^{-1}$

Entry	D ($cm^2 s^{-1}$)
$CHCl_3$	1.59×10^{-5}
BQ	1.43×10^{-5}
ZnTPP **17**	8.03×10^{-5}
Macroring **14**	3.56×10^{-5}
5mer **15**	3.68×10^{-5}
6mer **16**	3.45×10^{-5}

Further parameters for energy migration would be obtained from the value of Λ. When exciton migration is evaluated from the one-dimensional random walk model, the mean migration length L traveled as an exciton during its excited state lifetime is also evaluated as

$$L = (2\Lambda\tau_M)^{1/2} \tag{4.3.10}$$

Following descriptions, the rate parameters of energy migration were evaluated two approaches. A diffusion-controlled collisional process was adopted in **4.3.4**, and a diffusion-controlled long-distance electron transfer process was applied in **4.3.5**.

Furthermore, in **4.3.5** the critical radius $R_0{}^q$, wehere the rates of quenching reaction and decay of excited state of porphyrin are equal, was used from following equation (Förster, 1949)

$$R_0{}^q = 7.35 \times [BQ]_c{}^{-1/3} \tag{4.3.16}$$

where $R_0{}^q$ has the units of Å and defined from the critical concentration $[BQ]_c$ in M at the $I_0/I = 2 \ (= 1/0.5)$ in the Stern-Volmer equation (4.3.2). And $R_0{}^q = 48.3$ and 25.0 Å for the macroring **14** and ZnTPP **17**, respectively. Further $p = 0.5$ was put in the diffusion-controlled long-distance electron transfer process (**4.3.5**).

4.3.4   Diffusion-controlled Collisional Quenching

In this section the rate parameters of energy migration was evaluated by using the diffusion-controlled collisional process

$$k_{QM} = 4\pi N'(D_M + D_Q + \Lambda)pR \qquad (4.3.17)$$

When applying this process to ZnTPP **17**, caluculated $k_{QM} = 1.34 \times 10^{10}$ M^{-1} s^{-1} and experimental $k_q = 1.98 \times 10^{10}$ M^{-1} s^{-1} afford the value of p (= $k_q/k_{QM} \leq 1$) was 1.47 > 1.

This contradiction might indicate that the quenching process occurs not only the collisional but also the long-range electron transfer process, because other quenching reactions are trivial processes in these experiments.

4.3.5   Diffusion-controlled Long-range Electron Transfer Quenching

In this section the rate parameters of energy migration was evaluated by using the diffusion-controlled long-distance electron transfer process

$$k_{QM} = 2\pi N'(D_M + D_Q + \Lambda)R_0^q \qquad (4.3.18)$$

where $R_0^q = 25.0$ Å for the value of ZnTPP **17** was applied. In the case of ZnTPP **17**, caluculated k_{QM} was 2.11×10^{10} M^{-1} s^{-1} and the value of p was 0.94. This result indicates the validity of long-range electron transfer quenching process, and affords the energy migration coefficient $\Lambda \approx 0$ for ZnTPP **17**. From (4.3.18) and (4.3.10), the macroring

array **14** gave A = 1.3 × 10^{-4} cm²/s and the mean migration length L traveled as an

exciton during its excited state lifetime L = 73 Å, respectively. These values were

comparative to the aromatic crystal of phenanthrene, where A = 8.5 × 10^{-6} cm²/s, τ_M = 13

ns, and L = 47 and 81 Å for one- and three-dimensional random walk model, respectively

(Birks, 1970).

4.4 Conclusion

The rate parameters of energy migration in the macroring structure were evaluated by

using steady state spectroscopy. From the fluorescence quenching experiments, the

exciton delocalization was evaluated in the macroring array by the Stern-Volmer analysis

and the diffusion-controled dynamics. The macroring **14** and its component of the

slipped-cofacial dimer **12**, gave negligible shifts in both the Q bands absorption and the

fluorescence emission. Accordingly, the energy migration mechanism in the macroring

array might be described the incoherent hopping model rather than the coherent exciton

model. Meanwhile, taking into account for the closely chromophore separations and the

aromatic spacer between porphyrins, the contribution of coherent exciton type energy

migration must be considerable and departure from the Förster theory (Cho *et al.*, 2001).

Because some bis-zinc(II) gable porphyrin gave subpicosecond order (540 fs) energy

hopping between porphyrins (Yamazaki *et al.*, 1999), further photochemical

investigation utilizing ultrafast spectroscopy must be challenging.

Chapter 5   General Conclusion

5.1   Summary

In summary, the author succeeded in constructing the porphyrin macroring by interlocking 1,3-phenylene gable porphyrins by slipped-cofacial dimer formation without any protein matrices. This model must be a major milestone for further investigation to elucidate the mechanism of highly efficient light harvesting as well as the evolutional strategy of such ring structures in the natural photosynthetic system.

The principal findings of the studies described in this doctoral thesis are: (1) the applicability of the reorganization methods to macroring arrays, and (2) the reveal of the relation between structure and function in the macroring chromophores arrangement. These findings are very conscious of the natural photosynthetic light harvesting systems from our supramolecular chemical approach to the flagship of interdisciplinary studies.

The first applicability could be relevant to general formation process of higher ordered structure of protein and its reconstitution process such as a reconstitution of the LH1 complex (Miller *et al.*, 1987; Parkes-Loach *et al.*, 1988).

5.2   Outlook towards possible applications

The author presented an artificial light harvesting antenna complex mimicking the natural LH1, LH2, and LH3 complexes without protein matrices. The major difference is that the natural light harvesting complexes are drifting parallel within thylakoid membrane. These natural complexes are adapting for 2-dimensional photoelectron conversion system. Our findings of this studies elucidated such macroring arrays are effective light harvesting function also in homogeneous solution, i.e. 3-dimensional system.

In general it is difficult to assemble donor molecules in a highly concentrated state because of energy dissipation processes, e.g. concentration quenching, aggregation quenching and nondirectional energy transfer, in homogeneous solution. Notwithstanding closed chromophore-chromophore distances, natural antenna chlorophyll molecules accomplish energy migration and energy transfer very efficiently. These chlorophyll molecules are condensed in thylakoid membrane with highly ordered arrangements.

In the future, if one is allowed to wish to establish nano-scaled molecular devices, new strategies might be required further approaches, arranging each molecular assembly in ordered architecture and/or utilizing solid phase matrices: for 2-dimensional system such

as self-assembled monolayer and/or multilayer (Nomoto and Kobuke, 2002) and Langmuir-Blodgett membrane (Langmuir, 1918; Langmuir and Schaefer, 1937), for pseudo-2-dimensional system such as liposomal system with (Steinberg-Yfrach *et al.*, 1997) and/or without (Nagata *et al.*, 2001) lipids, and for 3-dimensional system such as micellar (Thomas, 1977) or dendritic system (Grayson *et al.*, 2001).

Towards such nano-scaled molecular devices from mimicking natural photosynthetic system, the macroring arrays presented here are possibly a good building block, because extremely long 1-dimensional molecular arrays could suffer from (1) the increased conformational heterogeneity in conformers, and (2) the aggregate formation (or partially insoluble arrays) in longer arrays (Kim *et al.*, 2001). The presented supramolecular approach has future prospects from a viewpoint of importance to prevent extra disordered aggregation between arrays, and to arrange each array in ordered geometry. Further elucidation of unveiling the relation between the structure and function of the natural light harvesting systems and applications for nano-scaled molecular devices utilizing macroring arrays should be a subject for active investigation.

A.1   Fluorescence Quenching Experiment

In this Appendix, the author will describe the photochemical processes in more details

based on *"Photophysics of Aromatic Molecules"* by Birks (Birks, 1970). At first elementary

processes are defined in **Figure A.1** and **Table A.1** and **A.2**.

Figure A.1   Schematic diagram of rate processes in exciplex formation, dissociation and quenching. Solid and broken lines are radiative and radiationless processes, respectively.

Table A.1   Unimolecular photochemical processes

Process	Description	Rate parameter
^{1}M processes		
^{1}M + hν $\longrightarrow$ ^{1}M*	S_0-S_1 absorption	—
^{1}M + hν $\longrightarrow$ ^{1}M**	S_0-S_p absorption	—
^{1}M* processes		
^{1}M* $\longrightarrow$ ^{1}M + hν_M	S_1-S_0 fluorescence	k_{FM}
^{1}M* $\longrightarrow$ ^{1}M	S_1-S_0 internal conversion	k_{GM}
^{1}M* $\longrightarrow$ ^{3}M*	S_1-T_1 intersystem crossing	k_{TM} $\Big\}$ k_{IM}
^{1}M* $\longrightarrow$ ^{3}M**	S_1-T_q intersystem crossing	
^{3}M* processes		
^{3}M* $\longrightarrow$ ^{1}M + hν_P	T_1-S_0 phosphorescence	k_{PT}
^{3}M* $\longrightarrow$ ^{1}M	T_1-S_0 intersystem crossing	k_{GT}
^{3}M* $\longrightarrow$ ^{1}M*	T_1-S_1 intersystem crossing	k_{MT}

$$k_M = k_{FM} + k_{IM} = k_{FM} + k_{TM} + k_{GM}$$

Table A.2 Heteropolar bimolecular interactions and exciplex processes

Process	Description	Rate parameter
Interactions		
$^1M + {}^1Q \longrightarrow {}^1(MQ)$	Complex formation	—
$^3M* + {}^1Q \longrightarrow {}^3E*$	Triplet exciplex formation	k_{XT}
$^1M* + {}^1Q \longrightarrow {}^1E*$	Singlet exciplex formation	k_{EM}
Complex and exciplex processes		
$^1(MQ) \longrightarrow {}^1M + {}^1Q$	Complex dissociation	—
$^1(MQ) + h\nu \longrightarrow {}^1E*$	Charge transfer absorption	—
$^1E* \longrightarrow {}^1M* + {}^1Q$	Singlet exciplex dissociation	k_{ME}
$^1E* \longrightarrow {}^1M + {}^1Q*$		k_{QE}
$^1E* \longrightarrow {}^1M + {}^1Q + h\nu_E$	Fluorescence	k_{FE}
$^1E* \longrightarrow {}^3E*$	Intersystem crossing	k_{XE}
$^1E* \longrightarrow {}^1M + {}^1Q$	Dissociative internal conversion	k_{GE}
$^1E* \longrightarrow {}^2M^+ + {}^2Q^-$	Dissociation into ions	k_{CE}
$^3E* \longrightarrow {}^3M* + {}^1Q$	Triplet exciplex dissociation	k_{TX}
$^3E* \longrightarrow {}^1M + {}^1Q + h\nu_X$	Phosphorescence	k_{PX}
$^3E* \longrightarrow {}^1M + {}^1Q$	Dissociative intersystem crossing	k_{GX}

$$k_E = k_{FE} + k_{IE} = k_{FE} + k_{GE} + k_{CE} + k_{XE} + k_{QE}$$

In 1919 Stern and Volmer obtained the relation

$$\Phi_{FM}/(\Phi_{FM})_0 = 1/(1 + k[Q]) \tag{A.1}$$

for fluorescence quenching in the gas phase. Where Φ_{FM} and $(\Phi_{FM})_0$ denote the porphyrin fluorescence quantum yield in the absence and presence of quencher molecules, respectively. And k and $[Q]$ denote the quenching coefficient and the molar concentration of the quencher molecule, respectively. In 1929 Valilov applied this relation to "dynamic quenching" in fluid solutions, and this relation was accepted by most other researchers in the field.

In 1924 Perrin, in discussing concentration quenching, introduced a concept of an active sphere, a volume of interaction around a quencher molecule such that a fluorescent molecule excited within this volume is quenched instantaneously, while fluorescent molecules excited outside this volume are unquenched. This concept provides a model of "static quenching" which does not require the formation of a bound complex between fluorescent molecule M and quencher molecule Q in the ground state. If v is the volume (in cm^3) of the active sphere of each quencher molecule and $n = [Q]N_A \times 10^{-3}$ is the number of quencher molecules in unit volume V (= 1 cm^3), the probability that a fluorescent molecule M will lie within an active sphere is

$$\rho = e^{-nv/V} \tag{A.2}$$

Hence on excitation the static quenching of the fluorescence is expressed by

$$\Phi_{FM}/(\Phi_{FM})_0 = e^{-k'[Q]} \qquad (A.3)$$
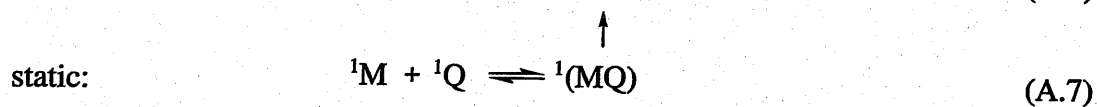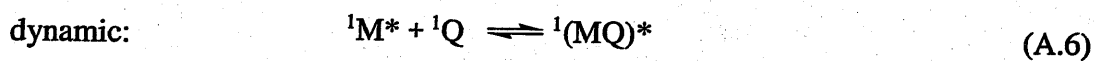
where

$$k' = vN' \qquad (A.4)$$

and N' is 1/1000 of the Avogadro's number N_A, $N' = N_A/1000$.

In 1931 Frank and Vavilov combined two relations (A.1) and (A.3) to obtain a more

general relation

$$\Phi_{FM}/(\Phi_{FM})_0 = e^{-k'[Q]}/(1 + k[Q]) \qquad (A.5)$$

Most of the subsequent models of fluorescence quenching that have been developed lead to

relations similar in form or approximate to (A.5). This relation accounts for some of the

controversy that has occurred about the nature of the quenching mechanism.

The distinction between dynamic and static quenching can arise from two possible modes

of formation of an excited complex,

dynamic: $\qquad$ $^1M^* + {}^1Q \rightleftharpoons {}^1(MQ)^*$ $\qquad\qquad$ (A.6)

$\qquad\qquad\qquad\qquad\qquad\qquad\qquad\qquad\uparrow$

static: $\qquad$ $^1M + {}^1Q \rightleftharpoons {}^1(MQ)$ $\qquad\qquad$ (A.7)

The molar equilibrium constant K_0 for the unexcited complex is independent of viscosity

and is given by

$$K_0 = [{}^1(MQ)^*]/([{}^1M][{}^1Q]) \qquad (A.8)$$

The fraction α of the incident light intensity I_0 which is absorbed by $^1(MQ)$ is given by

$$\alpha = \varepsilon'K_0[^1Q]/(\varepsilon + \varepsilon'K_0[^1Q]) \approx \varepsilon'K_0[^1Q]/\varepsilon = K[^1Q] \qquad (A.9)$$

where ε and ε' are the molar extinction coefficients of ^1M and $^1(MQ)$, respectively, at the wavelength of excitation.

The relevant rate equations are given by

$$d[^1M^*]/dt = (1 - \alpha)I_0 - (k_M + k_{EM}[^1Q])[^1M^*] + k_{ME}[^1E^*] \qquad (A.10)$$

$$d[^1E^*]/dt = \alpha I_0 + k_{EM}[^1Q][^1M^*] - (k_{ME} + k_E [^1E^*]) \qquad (A.11)$$

where the rate parameters are as defined in **Table A.1** and **A.2**. Under photostationary state conditions, the relative fluorescence quantum yield is given by

$$\Phi_{FM}/(\Phi_{FM})_0 = (1 - \alpha p)/(1 + \tau_M p k_{EM}[^1Q]) \qquad (A.12)$$

where $\tau_M = 1/k_M$ and

$$p = k_E/(k_{ME} + k_E) \qquad (A.13)$$

If $\alpha = 0$, (A.12) reduces to the Stern-Volmer relation

$$\Phi_{FM}/(\Phi_{FM})_0 = 1/(1 + \tau_M k_{QM}[^1Q]) \qquad (A.14)$$

where $k_{QM} = p k_{EM}$ and the quenching coefficient k (A.1) is given by

$$k = (\Phi_{FM}/(\Phi_{FM})_0 - 1)/[^1Q] = \tau_M k_{QM} \qquad (A.15)$$

If $\alpha = K[^1Q]$ is small, (A.12) may be written in the form, i.e. the dynamic and static quenching model

$$k = (\Phi_{FM}/(\Phi_{FM})_0 - 1)/[^1Q] = (K + \tau_M k_{QM}) + K\tau_M k_{QM}[^1Q] \qquad (A.16)$$

This relation predicts: (1) a linear increase in k with [Q], corresponding to a departure from

Stern-Volmer behavior, and (2) an increase in both the intercept and gradient of the k vs. [Q]

plot with increase in solvent fluidity $1/\eta$.

The quenching rate parameter is given by

$$k_{QM} = pk_{EM} = k_{EM} k_E/(k_{ME} + k_E) \qquad (A.17)$$

For a strong quencher ($p \approx 1$), $k_E \gg k_{ME}$ and hence

$$k_{QM} = k_{EM} \qquad (A.18)$$

i.e. the dynamic quenching is diffusion-controlled. For a weak quencher ($p \ll 1$) in a low

viscosity solvent, $k_E \ll k_{ME}$, and hence

$$k_{QM} = k_{EM} k_E/k_{ME} = K_E k_E \qquad (A.19)$$

where K_E is the equilibrium constant of the exciplex formation process (A.6). K_E and k_E are

independent of η, so that for a weak quencher k_{QM} is practically independent of η, except in

high viscosity solvents where k_{ME} is reduced sufficiently to become comparable with k_E.

The transient component of dynamic quenching arises from the second term in the

Smoluchowski expression for the rate parameter of a diffusion-controlled process

$$k_{diff} = 4\pi N'DpR(1 + pR(\pi Dt)^{-1/2}) \qquad (A.20)$$

While the treatment leading to (A.16) assumes steady state kinetics, i.e. that k_{QM} is

independent of t. Equation (A.20) shows that k_{QM} decreases initially with t before attaining

its steady state value. There is an initial transient quenching of those molecules adjacent to a

quencher molecule at the moment of excitation, while the subsequent quenching

corresponds to the photostationary, steady state condition. For the steady state diffusion-

controlled process, from (A.20)

$$k = k_{QM}\tau_M = 4\pi N'DpR\tau_M \qquad\qquad (A.21)$$

List of References

(1) Birks, J. B. *Photophysics of Aromatic Molecules*; Wiley-Interscience: London, 1970; Chapters 9–11.

(2) Blankenship, R. E. *Molecular Mechanisms of Photosynthesis*; Blackwell Science: Oxford, 2002.

(3) Brückner, C.; Sternberg, E. D.; Boyle, R. W.; Dolphin, D. *Chem. Commun.* **1997**, 1689–1690.

(4) Chang, M. C.; Callahan, P. M.; Parkes-Loach, P. S.; Cotton, T. M.; Loach, P. A. *Biochemistry* **1990**, *29*, 421–429.

(5) Cho, H. S.; Jeong, D. H.; Yoon, M.-C.; Kim, Y. H.; Kim, Y.-R.; Kim, D.; Jeoung, S. C.; Kim, S. K.; Aratani, N.; Shinmori, H.; Osuka, A. *J. Phys. Chem. A* **2001**, *105*, 4200–4210.

(6) Crossley, M. J.; Field, L. D.; Forster, A. J.; Harding, M. M.; Sternhell, S. *J. Am. Chem. Soc.* **1987**, *109*, 341–348.

(7) Deisenhofer, J.; Epp, O.; Miki, K.; Huber, R.; Michel, H. *J. Mol. Biol.* **1984**, *180*, 385–398.

(8) Förster, T. *Z. Elektrochem.* **1949**, *53*, 93–100.

(9) Gerasimchuk, N. N.; Mokhir, A. A.; Rodgers, K. R. *Inorg. Chem.* **1998**, *37*, 5641–5650.

(10) Grayson, S. M.; and Jean M. J. Fréchet, J. M. J. *Chem. Rev.* **2001**, *101*, 3819–3867.

(11) Gunter, M. J.; Mander, L. N. *J. Org. Chem.* **1981**, *46*, 4792–4795.

(12) Haycock, R. A.; Hunter, C. A.; James, D. A.; Michelsen, U.; Sutton L. R. *Org. Lett.* **2000**, *2*, 2435–2438.

(13) Heisenberg, W. *Z. Physik.* **1927**, *43*, 172–198.

(14) Ikeda, C.; Nagahara, N.; Yoshioka, N.; Inoue, H. *New J. Chem.* **2000**, *24*, 897–902.

(15) Ikeda, C. **2002**, *unpublished results*.

(16) Karrasch, S.; Bullough, P. A.; Ghosh, R. *EMBO J.* **1995**, *14*, 631–638.

(17) Kasha, M.; Rawls, H. R.; El-Bayoumi, M. A. *Pure Appl. Chem.* **1965**, *11*, 371–392.

(18) Kim, Y. H.; Jeong, D. H.; Kim, D.; Jeoung, S. C.; Cho, H. S.; Kim, S. K.; Aratani, N.; Osuka, A. *J. Am. Chem. Soc.* **2001**, *123*, 76–86.

(19) Knapp, S.; Vasudevan, J.; Emge, T. J.; Arison, B. H.; Potenza, J. A.; Schugar, H. J. *Angew. Chem. Int. Ed.* **1998**, *37*, 2368–2370.

(20) Kobuke, Y.; Miyaji, H. *J. Am. Chem. Soc.* **1994**, *116*, 4111–4112.

(21) Kobuke, Y.; Miyaji, H. *Bull. Chem. Soc. Jpn.* **1996**, *69*, 3563–3569.

(22) Koepke, J.; Hu, X.; Muenke, C.; Schulten, K.; Michel, H. *Structure* **1996**, *4*, 581–

597.

(23) Langmuir, I. *J. Am. Chem. Soc.* **1918**, *40*, 1361–1403.

(24) Langmuir, I.; Schaefer, V. J. *J. Am. Chem. Soc.* **1937**, *59*, 2075–2076.

(25) Lee, C.-H.; Lindsey, J. S. *Tetrahedron* **1994**, *50*, 11427–11440.

(26) Leighton, P.; Cowan, J. A.; Abraham, R. J.; Sanders, J. K. M. *J. Org. Chem.* **1988**, *53*, 733–740.

(27) Lepoittevin, B.; Dourges, M.-A.; Masure, M.; Hemery, P.; Baran, K.; Cramail, H. *Macromolecules* **2000**, *33*, 8218–8224.

(28) Li, J.; Ambroise, A.; Yang, S. I.; Diers, J. R.; Seth, J.; Wack, C. R.; Bocian, D. F.; Holten, D.; Lindsey, J. S. *J. Am. Chem. Soc.* **1999**, *121*, 8927–8940.

(29) Lindsey, J. S.; Schreiman, I. C.; Hsu, H. C.; Kearney, P. C.; Marguerettaz, A. M. *J. Org. Chem.* **1987**, *52*, 827–836.

(30) Littler, B. J.; Miller, M. A.; Hung, C.-H.; Wagner, R. W.; O'Shea, D. F.; Boyle, P. D.; Lindsey, J. S. *J. Org. Chem.* **1999**, *64*, 1391–1396.

(31) Littler, B. J.; Ciringh, Y.; Lindsey, J. S. *J. Org. Chem.* **1999**, *64*, 2864–2872.

(32) McDermott, G.; Prince, S. M.; Freer, A. A.; Hawthornthwaite-Lawless, A. M.; Papiz, M. Z.; Cogdell, R. J.; Isaacs, N. W. *Nature* **1995**, *374*, 517–521.

(33) McLuskey, K.; Prince, S. M.; Cogdell, R. J.; Isaacs, N. W. *Biochemistry* **2001**, *40*, 8783–8789.

(34) Medinger, T.; Wilkinson, F. *Trans. Faraday Soc.* **1965**, *61*, 620–630.

(35) Miller, J. F.; Hinchigeri, S. B.; Parkes-Loach, P. S.; Callahan, P. M.; Sprinkle, J. R.; Riccobono, J. R.; Loach, P. A. *Biochemistry* **1987**, *26*, 5055–5062.

(36) Mongin, O.; Schuwey, A.; Vallot, M.-A.; Gossauer, A. *Tetrahedron Lett.* **1999**, *40*, 8347–8350.

(37) Nagata, N.; Kugimiya, S.; Kobuke, Y. *Chem. Commun.* **2000**, 1389–1390.

(38) Nagata, N.; Kugimiya, S.; Kobuke, Y. *Chem. Commun.* **2001**, 689–690.

(39) Nomoto, A.; Kobuke, Y. *Chem. Commun.* **2002**, 1104–1105.

(40) Ogawa, K.; Kobuke, Y. *Angew. Chem. Int. Ed.* **2000**, *39*, 4070–4073.

(41) Osuka, A.; Maruyama, K. *J. Am. Chem. Soc.* **1988**, *110*, 4454–4456.

(42) Osuka, A.; Liu, B.-l.; Maruyama, K. *J. Org. Chem.* **1993**, *58*, 3582–3585.

(43) Parkes-Loach, P. S.; Sprinkle, J. R.; Loach, P. A. *Biochemistry* **1988**, *27*, 27 18–2727.

(44) Pickover, C. A.; Engelman, D. M. *Biopolymers* **1982**, *21*, 817–831.

(45) Quimby, D. J.; Longo, F. R. *J. Am. Chem. Soc.* **1975**, *97*, 5111–5117.

(46) Rao, P. D.; Littler, B. J.; Geier III, G. R.; Lindsey, J. S. *J. Org. Chem.* **2000**, *65*, 1084–1092.

(47) Rappé, A. K.; Casewit, C. J.; Colwell, K. S.; Goddard III, W. A.; Skiff, W. M. *J. Am. Chem. Soc.* **1992**, *114*, 10024–10035.

(48) Rexhausen, H.; Gossauer, A. *J. Chem. Soc., Chem. Commun.* **1983**, 275.

(49) Sanders, J. K. M. In *Comprehensive Supramolecular Chemistry*; Atwood, J. L., Davies, J. E. D., MacNicol, D. D., Vögtle, F., Eds.; Pergamon Press: Oxford, 1996, Vol. 9, pp 131–164.

(50) Sanders, J. K. M. In *The Porphyrin Handbook*; Kadish, K. M., Smith, K. M., Guilard, R., Eds.; Academic Press: New York, 2000a; Vol. 3, pp 347–368.

(51) Sanders, J. K. M.; Bampos, N.; Clyde-Watson, Z.; Darling, S. L.; Hawley, J. C.; Kim, H.-J.; Mak, C. C.; Webb, S. J. In *The Porphyrin Handbook*; Kadish, K. M., Smith, K. M., Guilard, R., Eds.; Academic Press: New York, 2000b; Vol. 3, pp 1–48.

(52) Savage, H.; Cyrklaff, M.; Montoya, G.; Kühlbrandt, W.; Sinning, I. *Structure* **1996**, *4*, 243–252.

(53) Scheuring, S.; Reiss-Husson, F.; Engel, A.; Rigaud, J.-L.; Ranck, J.-L. *EMBO J.* **2001**, *20*, 3029–3035.

(54) Sessler, J. L.; Hugdahl, J.; Johnson, M. R. *J. Org. Chem.* **1986**, *51*, 2838–2840.

(55) Seybold, P. G.; Gouterman, M. *J. Mol. Spectrosc.* **1969**, *31*, 1–13.

(56) Skvortsov, A. M.; Gorbunov, A. A. *Jounal of Chromatography* **1990**, *507*, 487–496.

(57) Smith, K. M. In *Porphyrins and Metalloporphyrins*; Smith, K. M., Ed.; Elsevier: Amsterdam, 1975a; pp 29–58.

(58) Smith, K. M. In *Porphyrins and Metalloporphyrins*; Smith, K. M., Ed.; Elsevier: Amsterdam, 1975b; pp 157–231.

(59) Solov'ev, K. N.; Tsvirko, M. P.; Gradyushko, A. T.; Kozhich, D. T. *Opt. Spektrosck.* **1972**, *33*, 871-878.; *Opt. Spectrosc. (USSR)* **1972**, *33*, 480–483.

(60) Steinberg-Yfrach, G.; Liddell, P. A.; Hung, S.-C.; Moore, A. L.; Gust, D.; Moore, T. A. *Nature* **1997**, *385*, 239–241.

(61) Svergun, D. I.; Barberato, C.; Koch, M. H. J. *J. Appl. Crystallogr.* **1995**, *28*, 768–773.

(62) Tabushi, I.; Sasaki, T. *Tetrahedron Lett.* **1982**, *23*, 1913–1916.

(63) Tabushi, I.; Kugimiya, S.; Kinnaird, M. G.; Sasaki, T. *J. Am. Chem. Soc.* **1985**, *107*, 4192–4199.

(64) Thomas, J. K. *Acc. Chem. Res.* **1977**, *10*, 133–138.

(65) Tomohiro, Y.; Satake, A.; Kobuke, Y. *J. Org. Chem.* **2001**, *66*, 8442–8446.

(66) Ueki, T.; Hiragi, Y.; Kataoka, M.; Inoko, Y.; Amemiya, Y.; Izumi, Y.; Tagawa, H.; Muroga, Y. *Biophysical Chemistry* **1985**, *23*, 115–124.

(67) van Oijen, A. M.; Ketelaars, M.; Köhler, J.; Aartsma, T. J.; Schmidt, J. *Science* **1999**,

285, 400–402.

(68) Walz, T.; Jamieson, S. J.; Bowers, C. M.; Bullough, P. A.; Hunter, C. N. *J. Mol. Biol.* **1998**, *282*, 833–845.

(69) Yamazaki, I.; Akimoto, S.; Yamazaki, T.; Shiratori, H.; Osuka, A. *Acta phys. Pol., A* **1999**, *95*, 105–120.

(70) Yang, S. I.; Seth, J.; Strachan, J.-P.; Gentemann, S.; Kim, D.; Holten, D.; Lindsey, J. S.; Bocian, D. F. *J. Porphyrins Phthalocyanines* **1999**, *3*, 117–147.

(71) Yu, G.-E.; Sinnathamby, P.; Prise, C.; Booth, C. *Chem. Commun.* **1996**, 31–32.

(72) Zhang, Y.; Wada, T.; Sasabe, H. *Chem. Commun.* **1996**, 621–622.

Acknowledgements

The work in this present thesis was carried out under the direction of Professor

Yoshiaki Kobuke of the division of Supramolecular Science in the Nara Institute of

Science and Technology (NAIST). The author would like to express heartfelt gratitude to

Professor Yoshiaki Kobuke for his passionate devotion to this project, especially not

only for research approach, but also for a scientific attitude of mind during his stirring

work. The author appreciates for being the first his laboratory member from being

accepted to this graduate school by grade skipping in 1998. Especially, during the course

of works of this thesis, the author has been experienced a phenomenal luck, *"Total*

Construction of Energy Conversion and Signal Transduction Systems in Biology" which

is one of the projects of the Core Research for Evolutional Science and Technology,

Japan Science and Technology Corporation, under Professor Yoshiaki Kobuke as the

research supervisor. And the author had chances meeting with many international

postdoctoral fellows and students, and having weekly reports in English. It would be

worth noting that the consistent preparations of academic theses for world wide

association in this laboratory are very salutary experience for the author.

The author is grateful for their commitment to Associate Professor Shin-ichi Kugimiya,

Assistant Professor Akiharu Satake, and Assistant Professor Kazuya Ogawa of the

Lists of Publications and Presentations

【学位論文の主たる部分を公表した論文】
(題目、全著者名、公表時期、雑誌名、巻、ページ)

"Hexameric Macroring of Gable-Porphyrins as a Light-Harvesting Antenna Mimic"
Ryoichi Hattori and Yoshiaki Kobuke
Journal of the American Chemical Society, 125 (9), 2372–2373

【国際学会発表】
(ポスター発表)

"Macroring Interlocking Gable Porphyrins as a Model of LH2-B850"
Ryoichi Hattori and Yoshiaki Kobuke
2nd International Conference on Porphyrins and Phthalocyanines, Kyoto TERRSA, July, 2002

【国内学会発表】
(ポスター発表)
「ビス-イミダゾリル置換ゲーブルポルフィリンによる相補的配位組織化」
服部良一、佐竹彰治、釘宮愼一、小夫家芳明
第 50 回錯体化学討論会、立命館大学 びわこ・くさつキャンパス、2000 年 9 月

(口頭発表)
「15,15'-ビスイミダゾリルゲーブルポルフィリンによる相補的配位組織化」
服部良一、佐竹彰治、釘宮愼一、小夫家芳明
日本化学会第 79 春季年会、甲南大学 岡本キャンパス、2001 年 3 月

「イミダゾール-亜鉛ポルフィリンの相補的配位組織化法による環状光捕集
複合体の構築」
服部良一、小夫家芳明
日本化学会第 81 春季年会、早稲田大学 西早稲田キャンパス、2002 年 3 月

「イミダゾリルポルフィリン環状組織体の構造と機能」
髙橋良一、小夫家芳明
日本化学会第 83 春季年会、早稲田大学 西早稲田キャンパス、2003 年 3 月

【その他発表】
（ポスター発表）
"Organization of 15,15'-Bisimidazolyl Gable Porphyrin Complementary Coordination"
Ryoichi Hattori, Akiharu Satake, Shin-ichi Kugimiya, and Yoshiaki Kobuke
湘南レクチャー（冬の部）、総合研究大学院大学 葉山キャンパス、2001 年 2 月

「イミダゾリルポルフィリンの亜鉛錯体による光合成モデルの構築」
服部良一、尾関秀謙、永田直人、小夫家芳明
分子複合系の構築と機能 第 2 回シンポジウム、日本科学未来館、2001 年 10 月